Neuron

Article

Multisensory coding of angular head velocity in the retrosplenial cortex

Highlights

- Angular head velocity (AHV) coding is widespread in the retrosplenial cortex (RSP)
- AHV cells maintain their tuning during passive motion and require vestibular input
- The perception of angular self-motion is improved when visual cues are present
- AHV coding is similarly improved when both vestibular and visual stimuli are used

Authors

Sepiedeh Keshavarzi, Edward F. Bracey, Richard A. Faville, ..., Stephen C. Lenzi, Tiago Branco, Troy W. Margrie

Correspondence

s.keshavarzi@ucl.ac.uk (S.K.), t.margrie@ucl.ac.uk (T.W.M.)

In brief

Keshavarzi et al. report that mouse retrosplenial cortical neurons can reliably track the direction and speed of head turns in complete darkness by relying on vestibular information. Addition of visual input improves perception of angular self-motion and increases the accuracy of this cortical head motion signal.

Keshavarzi et al., 2022, Neuron *110*, 532–543
February 2, 2022
https://doi.org/10.1016/j.neuron.2021.10.031

CellPress

CellPress
OPEN ACCESS

Neuron

Article

Multisensory coding of angular head velocity in the retrosplenial cortex

Sepiedeh Keshavarzi,[1,*] Edward F. Bracey,[1,3] Richard A. Faville,[1] Dario Campagner,[1,2] Adam L. Tyson,[1] Stephen C. Lenzi,[1] Tiago Branco,[1] and Troy W. Margrie[1,4,*]

[1]Sainsbury Wellcome Centre for Neural Circuits and Behaviour, University College London (UCL), 25 Howland Street, London W1T 4JG, United Kingdom

[2]Gatsby Computational Neuroscience Unit, University College London (UCL), 25 Howland Street, London W1T 4JG, United Kingdom

[3]Present address: Neurobehavioural Dynamics Lab, Institute for Neuroscience, D-HEST, Swiss Federal Institute of Technology / ETH Zürich, Zürich 8603, Switzerland

[4]Lead contact

*Correspondence: s.keshavarzi@ucl.ac.uk (S.K.), t.margrie@ucl.ac.uk (T.W.M.)

https://doi.org/10.1016/j.neuron.2021.10.031

SUMMARY

To successfully navigate the environment, animals depend on their ability to continuously track their heading direction and speed. Neurons that encode angular head velocity (AHV) are fundamental to this process, yet the contribution of various motion signals to AHV coding in the cortex remains elusive. By performing chronic single-unit recordings in the retrosplenial cortex (RSP) of the mouse and tracking the activity of individual AHV cells between freely moving and head-restrained conditions, we find that vestibular inputs dominate AHV signaling. Moreover, the addition of visual inputs onto these neurons increases the gain and signal-to-noise ratio of their tuning during active exploration. Psychophysical experiments and neural decoding further reveal that vestibular-visual integration increases the perceptual accuracy of angular self-motion and the fidelity of its representation by RSP ensembles. We conclude that while cortical AHV coding requires vestibular input, where possible, it also uses vision to optimize heading estimation during navigation.

INTRODUCTION

Whether foraging for food or taking refuge from danger, the survival of most animals depends on their knowledge of current location and heading direction. Such cognitive capacity requires not only an accurate estimation of the momentary heading direction, but also the ability to update it with subsequent head turns as the animal moves through space (Blair and Sharp, 1995; Laurens and Angelaki, 2018; McNaughton et al., 1991; McNaughton et al., 1995). Head direction cells, identified in various animals ranging from insects to primates, are tuned to the azimuthal direction of an animal's head in its environment (Robertson et al., 1999; Seelig and Jayaraman, 2015; Taube et al., 1990a, 1990b), and are thought to provide an internal representation of the sense of direction (Butler et al., 2017; Frohardt et al., 2006). It is widely accepted that the updating of this heading direction signal arises from angular velocity integration (Blair and Sharp, 1995; Green et al., 2017; Laurens and Angelaki, 2018; McNaughton et al., 1991; McNaughton et al., 1995; Turner-Evans et al., 2017), with theoretical models of head direction computation requiring the existence of neurons that encode angular head velocity (AHV) (Bassett and Taube, 2001; Sharp et al., 2001), and neurons with conjunctive head direction and AHV tuning (Blair, 1995; Redish et al., 1996; Skaggs et al., 1995; Zhang, 1996).

In theory, AHV information can be obtained from multiple internal and external sources, including vestibular signals, efference copy of motor commands, proprioceptive input from eye and neck muscles, and optic flow; yet whether and how these motion cues contribute to cortical AHV coding during navigation remains unknown. On the one hand, perceptual experiments in humans and non-human primates suggest that the combination of vestibular and visual stimuli improves estimates of heading during passive translation (Butler et al., 2010; DeAngelis and Angelaki, 2012; Fetsch et al., 2011; Fetsch et al., 2009; Gu et al., 2008). On the other hand, for instance in noncortical areas, vestibular signals are suggested to be either completely inhibited or only weakly active during self-generated movements (Cullen, 2014; Cullen and Taube, 2017; Sharp et al., 2001; Shinder and Taube, 2014). In spite of this, successful path integration and head direction tuning in the thalamus appears to require an intact vestibular system (Muir et al., 2009; Shinder and Taube, 2011; Wallace et al., 2002).

A major obstacle impeding progress in understanding cortical AHV coding and other egocentric elements of spatial navigation, is the inability to precisely disentangle the contribution of these various sensory cues in freely moving animals. Conversely, while head-fixed experiments allow quantitative control of sensory stimuli, the direct relevance of signals recorded in such preparations to natural navigation is unclear. Here, we have identified

cortical AHV cells during free exploration and determined their response properties to isolated and conjunctive sensory stimuli. We have focused on AHV cells in the RSP since it is a multisensory cortical region that forms part of the head direction network and encodes various spatial and movement-related information (Alexander et al., 2020; Alexander and Nitz, 2015, 2017; Chen et al., 1994a, 1994b; Chinzorig et al., 2020; Cho and Sharp, 2001; Jacob et al., 2017; Mao et al., 2017; Mao et al., 2020; Powell et al., 2020; Vale et al., 2020; van Wijngaarden et al., 2020; Vann et al., 2009; Vedder et al., 2017; Vélez-Fort et al., 2018). Notably, studies on both rodents and humans suggest that the RSP is critically involved in spatial orientation and self-motion-guided navigation (Chrastil et al., 2017; Chrastil et al., 2015; Cooper et al., 2001; Cooper and Mizumori, 1999, 2001; Elduayen and Save, 2014; Maguire, 2001; Takahashi et al., 1997; Whishaw et al., 2001), and recent work suggests that it can provide head-motion information to the visual cortex (Vélez-Fort et al., 2018). A growing number of studies in recent years has advanced our knowledge of allocentric head direction representation in the RSP and the potential role of this region in processing landmark information (Auger et al., 2012; Bicanski and Burgess, 2016; Fischer et al., 2020; Jacob et al., 2017; Page and Jeffery, 2018). However, despite increasing evidence for self-referenced computations in the RSP (Alexander et al., 2020; Vale et al., 2020; van Wijngaarden et al., 2020), the extent to which self-motion information such as AHV is represented in this region and the underlying mechanisms remains unexplored.

RESULTS

Extensive network of AHV cells in the RSP during free exploration

Using chronically implanted high-density silicone probes (Neuropixels and Neuronexus), RSP neurons (n = 359 single units in 5 mice, right hemisphere) were first recorded from mice while they freely explored a circular arena (Figures 1A and 1B) under both light and dark conditions. Head and body movements were tracked in 2D (horizontal plane of motion), and—based on their tuning function—neurons were classified as encoding one or a combination of three navigational properties: heading direction, AHV, and linear locomotion speed (Figures 1C–1H). Neurons were classified as head direction tuned if (1) the distribution of their firing rate as a function of head direction was statistically non-uniform (Rayleigh p value < 0.01), (2) their mean Rayleigh vector length was >99th percentile of the population null distribution, and (3) these criteria were met during two recording epochs separated by at least 20 min. AHV and speed scores were defined as the magnitude of correlations (Pearson's r) between the neuron's firing rate and the horizontal angular head velocity or linear locomotion speed, respectively. Neurons were defined as AHV or speed tuned if these scores were >95th percentile of the shuffled distribution generated by shifting spike times (see STAR Methods).

Similar to previous reports (Chen et al., 1994b; Cho and Sharp, 2001), approximately 10% of RSP neurons were identified as classic head direction cells (36/359; Figures 1F–1H). Strikingly, the majority of recorded neurons were modulated by self-motion parameters including AHV (224/359; Figures 1D, 1G, 1H, and S1A), and—to a lesser degree—locomotion speed (182/359; Figures 1E, 1G, 1H, and S1A). In addition, many head direction cells also conjunctively encoded AHV (22/36; Figures 1G and S1B). Identified AHV- and speed-tuned cells had stable tuning throughout the recording session (Figure S1C) with significantly higher stability indices (see STAR Methods) than shuffled distributions (p (AHV) = 3.2e-168, p (locomotion speed) = 2e-79, Kolmogorov–Smirnov test; Figure S1D). Moreover, consistent with previous data (Alexander et al., 2020; Laurens et al., 2019), theta-rhythmic firing was largely absent among RSP neurons with no difference between the three tuned populations (Theta-modulated cells: n (all cells) = 23/359, 6.4% ; n (AHV) = 17/224, 7.6%; n (locomotion speed) = 16/182, 8.8%; n (head direction) = 1/36, 2.8%; Figures S1E and S1F).

Regarding the range used to construct angular head velocity tuning curves (-80°/s to 80°/s; see STAR Methods), the spiking activity of AHV cells was linearly or near-linearly modulated by the speed of head turns, with the majority being positively correlated with angular speed (193/224; Figure 1D). In 57% of these cells (128/224), speed modulation was unidirectional, meaning that their firing rate was significantly correlated with the speed of either right or left head turns (Figure 1D, top), with no apparent preference for either direction at the population level (Figure 1H, right). Additionally, a small fraction of cells (3/224; Figure 1D, top-right) showed a positive speed correlation in one direction and a negative correlation in the other. Thus, AHV cells in the RSP appear to represent both the speed and the direction of angular head movements.

AHV-tuned neurons were found across all cortical layers in both dysgranular (n = 109/224 AHV cells, percentage of all recorded neurons: layer 2/3 = 64%, layer 5 = 57%, layer 6 = 61%) and granular (n = 115/224 AHV cells, percentage of all recorded neurons: layer 2/3 = 53%, layer 5 = 67%, layer 6 = 68%) divisions of the RSP (Figures 1C, S1G, and S1H), and consisted of both putative excitatory (121/224) and inhibitory (103/224) cell types (Figure S2), suggesting that AHV representation in the RSP is widespread, distributed across regions, and more prevalent than previously reported (Cho and Sharp, 2001; Laurens et al., 2019).

AHV tuning is maintained during passive motion and dependent on vestibular input

To distinguish the contribution of various external and internal motion cues to AHV signaling, we tracked the same units (Figure S3) from the open field arena to a body- and head-restrained paradigm (Figure 2A) where we could parametrically vary vestibular and visual stimuli and exclude inputs from locomotion, neck-on-body proprioception, and voluntary head movements. To determine the contribution of vestibular signals, we first tested whether in the absence of visual input, AHV cells recorded in the open field could encode the angular velocity of horizontal passive rotation. Out of 90 AHV cells that were successfully identified in head-fixed recordings, the spiking rate of 72 cells (80%) was significantly correlated with the velocity of passive rotation in the dark. Interestingly, despite the initiation of complex head and body movements during free exploration as compared to head-fixed horizontal rotations, a substantial fraction of AHV cells (48.8% ± 6.6%, n = 5 mice, 12 recording sessions) had similar tuning to passive rotation

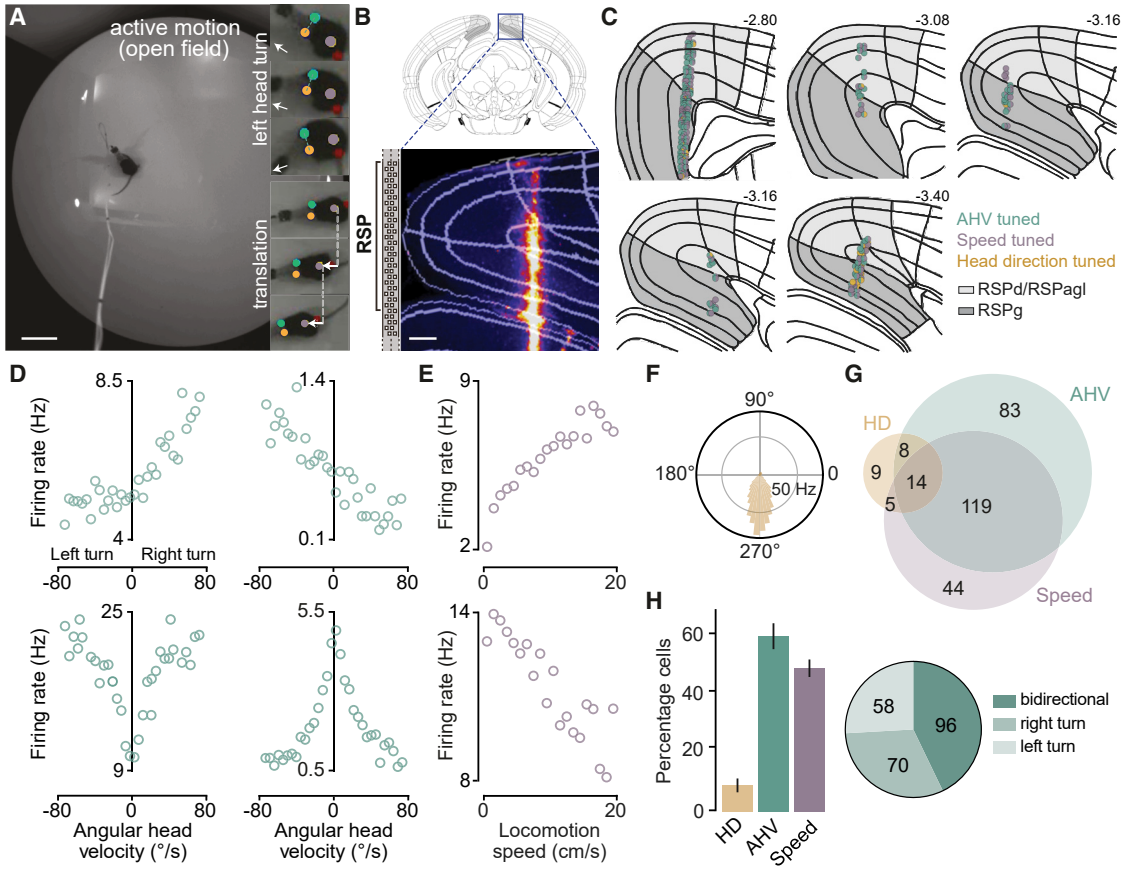

Figure 1. Extensive network of AHV cells in the RSP during free exploration

(A) A video frame showing the open field arena used for exploration. Insets, video frames showing a left head turn (top three) and locomotion (bottom three) tracked using the position of ears and the body. Arrows indicate head direction (top three) and linear displacement (bottom three). Scale bar: 10 cm.

(B) Top: schematic of a coronal brain section with RSP highlighted in gray, Bottom: inset shows a coronal 2P image of the Neuropixels probe track marked with DiI. Scale bar: 200 μm.

(C) Schematic showing chronic recording sites in all 5 mice. Circles indicate the approximate location of cells tuned to AHV, speed, and heading direction (HD) within the dysgranular/agranular (light gray) and granular (dark gray) regions of the RSP. Numbers are distances from Bregma (in mm). All schematics and boundary outlines are based on the Allen Mouse Brain Atlas (Wang et al., 2020).

(D) Tuning plots of four types of AHV cells: a unidirectional cell with positive speed correlation (top-left), a cell with opposite correlations (top-right), and two bidirectional cells with positive (bottom-left) and negative (bottom-right) speed correlations.

(E) Tuning plots of two representative speed cells showing positive (left) and negative (right) correlations with locomotion speed.

(F) An example HD cell in the RSP. Visual landmark was located at 180°.

(G) Venn diagram showing cells tuned to HD, AHV, and linear locomotion speed (n total = 359).

(H) Left: summary data (mean ± SEM, n = 5 mice, 12 recordings) showing percentage of cells that were tuned to HD, AHV, or locomotion speed. Right: pie chart represents proportion of AHV cells (n = 224) with bidirectional and unidirectional (right or left turn) tuning. See also Figures S1 and S2.

(Figures 2B–2D), and this similarity was observed in all AHV tuning types (Figure S4). Considering the absence of voluntary head and neck movements and behavioral confounds such as postural signals (Mimica et al., 2018) during passive rotations, these findings indicate that, at least in the dark, vestibular input is a major source of AHV cells' activity. In support of this, bilateral kanamycin injections into the horizontal and posterior semicircular canals (Figure S5), which lead to hair cell damage and death in these canals and thus reduction of vestibular signals, significantly reduced rotation-evoked, but not visual responses (Figure 2E), as well as the magnitude of angular velocity correlations (Lesioned: median velocity Pearson's r = 0.26, IQR = 0.12 – 0.42, n = 4 mice, 7 recordings, 313 cells; Control: median velocity Pearson's r = 0.39, IQR = 0.2 – 0.6, n = 10 mice, 19 recordings, 676 cells; p = 4.78e-33, Wilcoxon rank-sum test; Figure 2F). It is plausible that the effect of vestibular lesions are indirectly caused by the suppression of vestibulo-ocular reflex (VOR)-driven eye movements. We thus further determined the extent to which RSP neuronal activity is modulated with eye position during VOR resets, and found a very small fraction of RSP neurons with eye-movement-correlated activity (cells with significant pupil position correlations in the dark: temporal = 8/101, nasal = 6/101, n = 3 mice; Figure S6). These findings not only highlight the contribution of vestibular cues to AHV signaling, but also show that eye movement-related signals are not significant drivers of AHV tuning.

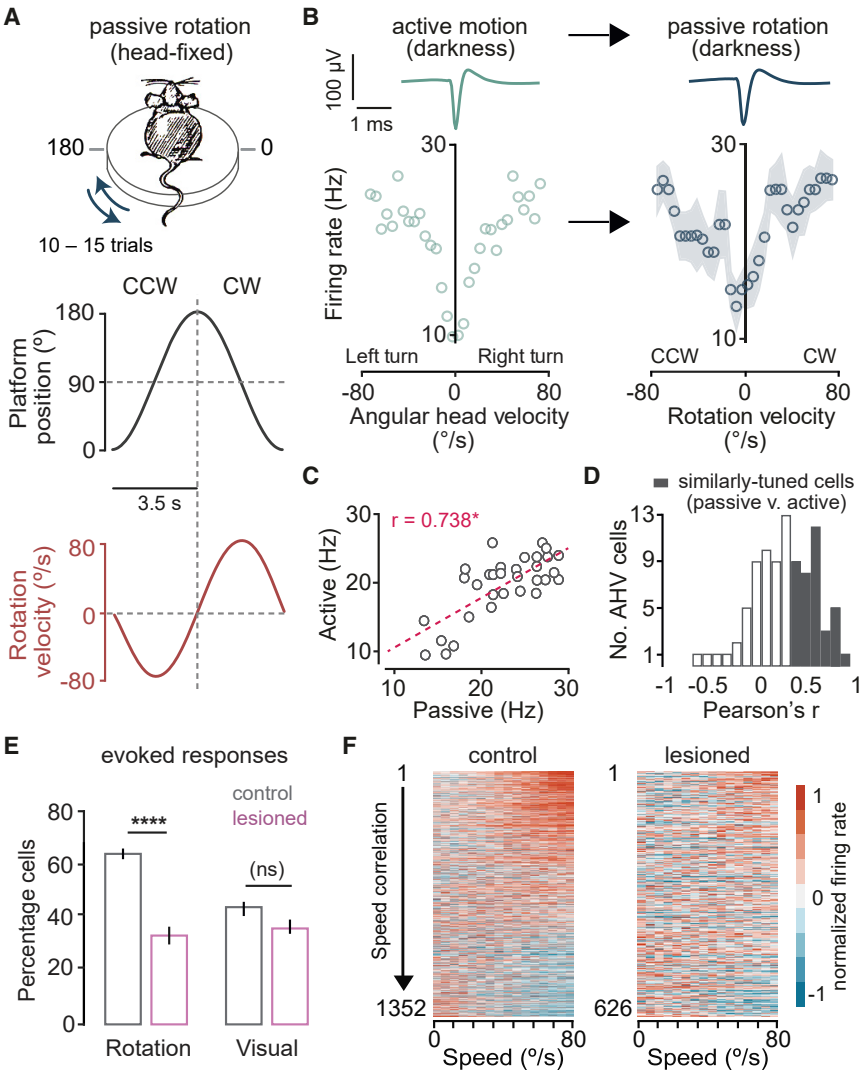

Figure 2. AHV cells maintain their tuning during restrained passive motion

(A) Top: schematic of the design for passive rotation experiments. Centre and bottom: position and velocity profile of an individual rotation stimulus.

(B) Tuning plots of a bidirectional AHV cell recorded initially in the open field (left) and subsequently during passive rotation (right) in darkness. Top: average trace of this unit's spike waveform recorded under each condition. Circles and shaded area on the right show trial-averaged firing rates (12 trials) and SEM, respectively.

(C) Firing rate at each velocity bin for the cell shown in (B) plotted for active versus passive conditions. * Pearson's r >95th percentile of the null distribution = similarly tuned.

(D) Distribution of Pearson's r of correlation between passive and active tuning curves for all tracked AHV cells in the dark (n = 90).

(E) Summary data (mean ± SEM; Control: n = 10 mice, 20 recordings, 676 cells; Lesioned: n = 4 mice, 7 recordings, 313 cells) showing the percentage of cells with evoked responses (significant increase or decrease in firing rate relative to baseline) to rotation in darkness or to full-field visual flow. ****p = 2.8e-5, (ns) p = 1, Kruskal-Wallis with Dunn's test.

(F) Heatmaps show baseline-subtracted, normalized average firing rate as a function of rotation speed in darkness for controls (left) and lesioned animals (right). Each pair of rows represents an individual neuron's response to clockwise (CW) and counter-clockwise (CCW) rotations. Neurons are sorted by the magnitude of speed correlations (Pearson's r) averaged over the two directions. See also Figures S3–S6.

Vestibular and optic flow input converge onto AHV cells

Since the RSP is extensively connected with visual areas (Oh et al., 2014; Van Groen and Wyss, 1990, 1992), it is conceivable that, when available, optic flow information could also contribute to motion representation by AHV cells. To test this, we recorded from AHV cells during both vestibular stimulation (passive rotation in the dark, Figure 3A) and full-field visual motion stimulation when the animal was stationary (Figure 3B). The visual motion stimulus, which was projected onto a cylinder surrounding the animal, had the same velocity profile as the rotation stimulus. Although visually evoked responses were weaker than those evoked by vestibular stimulation (rotation modulation index: median (vestibular) = 0.29, IQR = 0.13 – 0.6, median (visual) = 0.19, IQR = 0.08 – 0.42, n = 120 AHV cells, p = 2.4e-7, Wilcoxon signed rank test), many AHV cells (52/120) increased or decreased their spiking activity in response to both stimuli, and were modulated by the speed (62/120) and—to a lesser degree—the direction (22/120) of both (Figures 3A and 3B).

Optic flow input increases the gain and signal-to-noise ratio of AHV signaling

While it is well established that visual inputs convey landmark information to head direction cells to maintain their tuning (Goodridge and Taube, 1995; Yoder et al., 2015; Zugaro et al., 2003), the contribution of vision to AHV coding remains unclear. The combined vestibular-visual activation could theoretically provide a moment-to-moment AHV signal based on both internal and external cues. In agreement with this, we observed that in freely moving mice, a significantly larger fraction of RSP cells are tuned to AHV in presence of visual signals than in the dark (dark = 192/359, light = 223/359, p = 0.02, Fisher's exact test). Notably, addition of visual input increased the slope of angular head velocity/spiking rate relationship and the magnitude of speed correlations (Figures 3C–3E), suggesting that visual signals increase the gain and improve the signal-to-noise ratio of AHV coding. Considering this increase in the dynamic range of AHV tuning when both sensory cues are available, we hypothesized that vestibular-visual integration could markedly improve the fidelity of angular velocity representation by RSP network and generate a reliable estimate of angular self-motion.

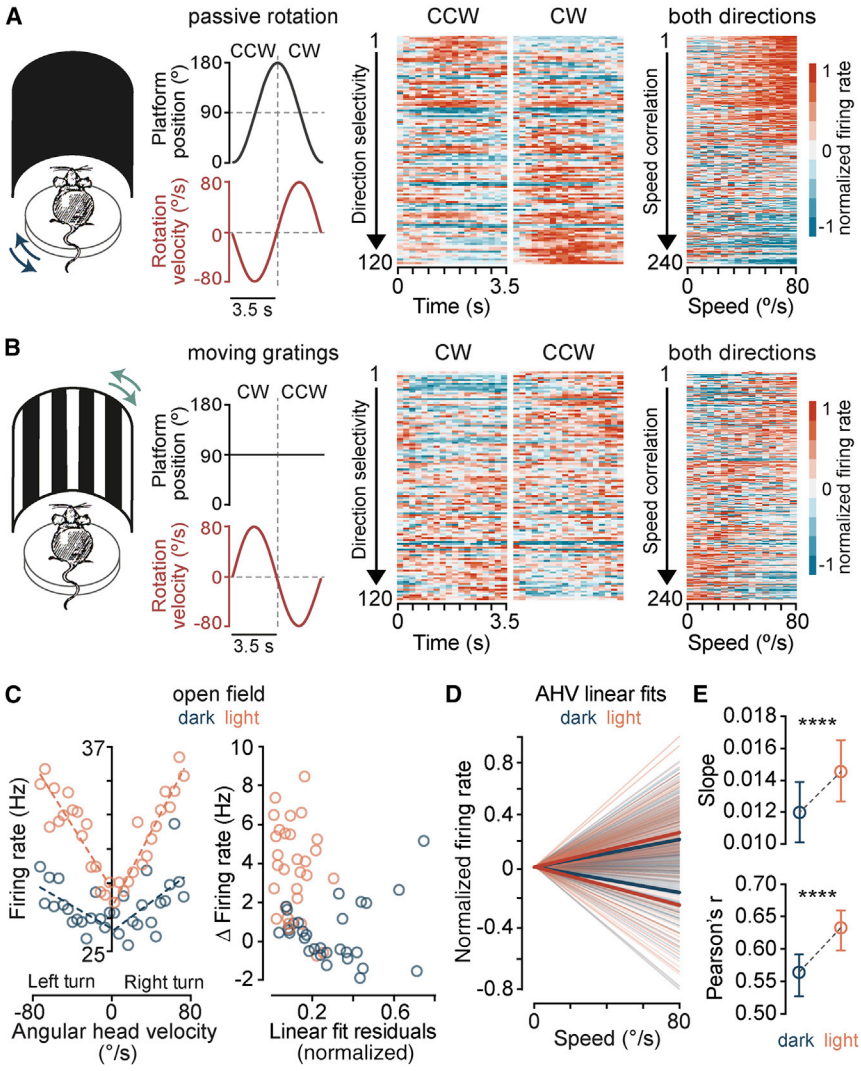

Figure 3. Vestibular and optic flow input converge onto AHV cells

(A) Left: experimental design for vestibular stimulation. Traces show the position (black) and velocity (red) of the rotating platform. Centre: firing rate heatmaps of all tracked AHV cells during CW and CCW rotations in darkness. Rows show baseline-subtracted, normalized average firing rate of all neurons sorted by their direction selectivity index (area under the direction ROC curve; see STAR Methods). Right: baseline-subtracted, normalized average firing rate of all neurons as a function of rotation speed. Each pair of rows shows an individual neuron's response to CW and CCW rotations. Neurons are sorted by the magnitude of speed correlations (Pearson's r), averaged over the two directions.

(B) Left: the rotation platform was stationary (black trace) while a surround vertical grating was rotated with the same velocity profile as the vestibular stimulus in (A) (red trace). Centre and right: same as in (A) but for the visual stimulus.

(C) Left: tuning curves of an example AHV cell recorded in the open field in darkness and in light. Dashed lines represent linear fits. Right: for the same cell, firing rate difference between the first and all other velocity bins is plotted against the residual of the linear fit.

(D) Population data showing linear fits for all AHV cells and for each direction in darkness and in light. Thick lines are averaged fits for either positive or negative correlations.

(E) Summary data (median and 95% CI, n = 272 AHV cells) showing the overall change between dark and light conditions. ****p (slope) = 2.9e-11, ****p (Pearson's r) = 1.2e-6, Wilcoxon signed rank test.

Combined vestibular and visual stimuli improve the perceptual accuracy of angular self-motion

To address this hypothesis at the behavioral and network level, we took advantage of our head-restrained paradigm which allows the separation and quantitative control of visual motion and vestibular information. We could therefore examine whether a switch to using visual flow instead of vestibular signals occurs when vision is available, or whether the two self-motion inputs are integrated for perception and neuronal encoding. First, we trained mice in a go/no-go task to discriminate between their own angular speeds, either in the dark or in presence of optic flow information (Figures 4A and 4B). In complete darkness, mice could differentiate between pairs of rotation stimuli (Vélez-Fort et al., 2018) that differed by at least 20°/s in their peak speed (mean ± SEM discrimination accuracy of 5 blocks: 10°/s v. 10°/s = 49.6% ± 3.7% compared to 10°/s v. 30°/s = 74.6% ± 4.6%, n = 5 mice, p = 0.02, one-way ANOVA with Holm-Sidak's test; Figure 4C). Presenting a static vertical grating, to provide optic flow in addition to vestibular stimulation (Figure 4B, center), lowered the discrimination threshold from 20°/s to 10°/s (10°/s v. 10°/s compared to 10°/s v. 20°/s: p (vestibular) = 0.09, p (vestibular + visual) = 0.01, one-way ANOVA with Holm-Sidak's test; Figure 4C), and significantly increased the perceptual accuracy of self-motion (Figures 4C and 4E). Notably, mice performed substantially worse in a pure visual task, which consisted of pairs of visual motion stimuli moving horizontally past the animal with the same speed profiles as the rotation stimulus pairs (Figures 4B, right, 4D, and 4E). The improved self-motion discrimination performance in presence of the static visual cue is therefore not due to sole reliance on visual flow information, but rather requires the combination of vestibular and visual signals. Furthermore, the improved performance under "vestibular + visual" condition could not be attributed to learning with task progression since subsequent performance on the vestibular alone task returned to the same level as initially observed (Figure S7). These results, obtained for the first time in rodents, demonstrate the behavioral significance of concomitant vestibular-visual input and are consistent with human data showing improved perception of angular self-motion when multisensory cues are made available (Jürgens and Becker, 2006; Prsa et al., 2012).

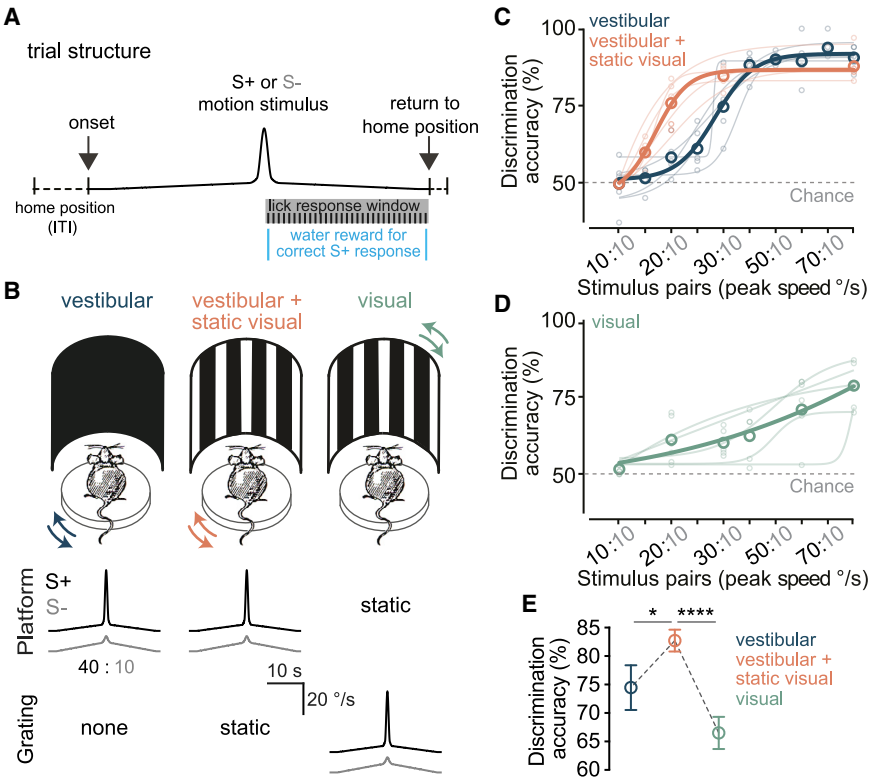

Figure 4. Combination of vestibular and visual stimuli improves perceptual accuracy of angular self-motion

(A) Schematic of trial structure for the go/no-go speed discrimination task. The trace illustrates a generic rotation velocity profile (motion stimulus) for an individual trial. Stimulus duration = 32.2 s, inter-trial interval (ITI) = 5 s.

(B) Schematic of the three experimental conditions. Mice either discriminated speed of self-motion in the dark (vestibular, left) or in presence of a static visual stimulus (vestibular + static visual, center). Under the third condition (visual, right), the rotation platform was kept stationary while the grating rotated to provide visual motion stimulation with the same speed profile used in the previous two conditions (center and bottom rows).

(C) Accuracies of self-motion speed discrimination for all stimulus pairs (n = 5 mice, average of 5 blocks). Small and large circles represent individual animals and group averages, respectively. Lines are sigmoid fits.

(D) As in (C) but for visual motion discrimination.

(E) Mean (±SEM) discrimination accuracies of all stimulus pairs that were tested under the three conditions (20:10, 30:10, and 80:10) in all 5 mice. *p = 0.014, ****p = 1.1e-5, one-way ANOVA with Holm-Sidak's test. See also Figure S7.

AHV cells show heterogenous vestibular-visual response properties

We next sought to answer whether the activity of ensembles of RSP neurons under such multimodal condition similarly improves the fidelity of angular velocity coding, thus mirroring the psychometric data. We first employed single-cell decoding methods on AHV cells that were tracked in the head-restrained experiments (n = 120). Decoding with ROC revealed a range of response types across the population, with some neurons discriminating the direction (clockwise versus counter-clockwise) and/or the speed of rotations exclusively in the dark, some only in presence of a static visual stimulus, and others under both conditions (Figures 5A–5C). Despite this heterogeneity, the total number of cells that could discern the angular speed (vestibular = 36/120, vestibular + visual = 51/120) and the average discriminability (area under ROC = AUC; Figure 5D) increased in the presence of optic flow compared to in darkness. For rotation direction, the effect of multisensory combination was only evident at the onset of motion (Figure 5E, left, first 500 ms of rotation), with no significant difference in proportion of direction-discriminating cells (entire rotation window: vestibular = 33/120, vestibular + visual = 34/120, p = 1; first 500 ms: vestibular = 5/120, vestibular + visual = 22/120, p = 8e-4, Fisher's exact test) or discriminability between the two conditions when longer epochs of the rotation stimulus (3.5 s) were considered (Figure 5E, right). We reasoned that the observed functional diversity at the level of individual AHV cells might enhance the efficiency of the population code, thus allowing the RSP ensembles to use all relevant available sensory cues to generate the most accurate representation of self-motion.

Vestibular-visual combination increases the fidelity of self-motion representation by AHV cell populations

To investigate this, we used linear discriminant analysis (LDA) to decode the direction and speed of rotation from the population activity. First, by pooling all RSP neurons recorded in the dark into pseudo-populations of increasing size, we found that the decoder could reliably predict these angular velocity parameters with ensembles of fewer than 100 neurons (Figures 6A and 6B). Importantly, vestibular lesions significantly reduced the accuracy of decoding both direction (mean ± SEM direction decoding accuracy: Lesioned = 66.6% ± 2.4%, n = 4 mice; Control = 96.1% ± 1.6%, n = 10 mice; 10 – 300 pooled neurons, p = 1.7e−9, Student's t test; Figure 6A) and angular speed (mean ± SEM speed decoding accuracy: Lesioned = 55.3% ± 0.7%, Control = 70.5% ± 2.6%, all speed pairs, p = 0.0001, Student's t test; Figure 6B). These data suggest that a small ensemble of RSP neurons can reliably report angular head velocity in the dark using vestibular input alone. Next, using the same method on all tracked AHV cells, we compared decoding accuracies under the three experimental conditions. As predicted, adding a static vertical grating during rotation enhanced the performance of the decoder and, similar to the perceptual task, this improved performance could not be attributed to vision alone (Figures 6C and 6D); however, in line with results from the ROC analysis, the improvement in decoding direction was only evident at the beginning of motion (mean ± SEM direction

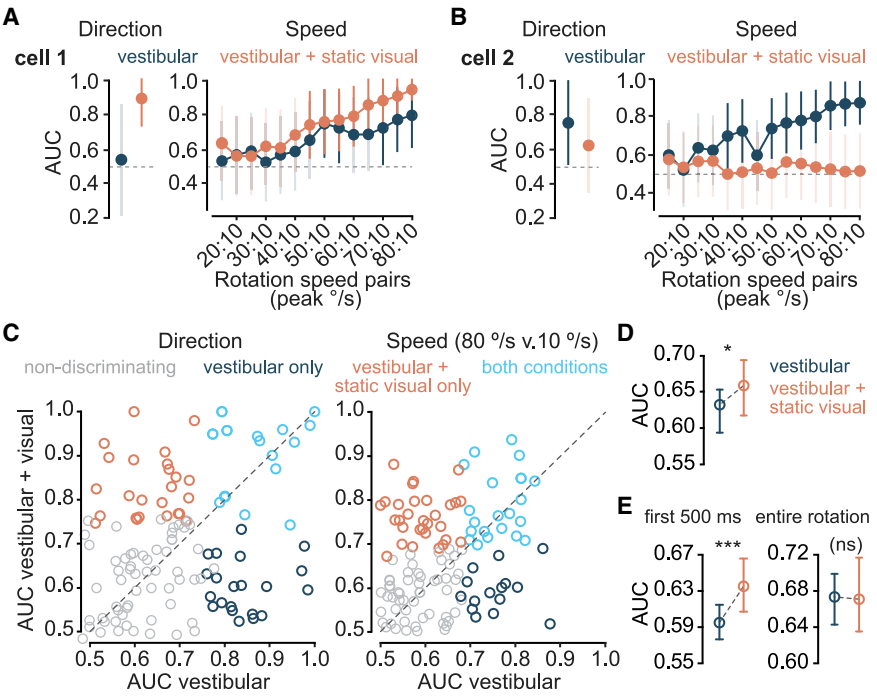

Figure 5. Heterogenous vestibular-visual response properties of AHV cells

(A) Left: normalized AUCs for a cell that discriminates direction of rotation in presence of visual signals (vestibular + visual) but not in the dark (vestibular). Right: normalized AUCs for speed ROC showing improved speed discrimination under the vestibular-visual condition. Transparent and solid error bars indicate 99% CIs within and above chance level, respectively.

(B) Similar to (A), but for a different cell that discriminates the direction and speed of rotation only in the dark.

(C) Scatterplot of AUCs for direction (left) and speed (right) discrimination. AUCs under vestibular-visual condition (rotation with static visual stimulus) are plotted against AUCs under vestibular condition (rotation in the dark). Each circle represents one tracked AHV cell (n = 120). Direction ROC curves compared the firing rates between CW and CCW rotations. Speed ROC curves compared the firing rates between the speed bin that peaked at 10°/s and successive speed bins (15°/s–80°/s peak). Grey circles show non-discriminating cells. Dark blue and orange represent, respectively, cells that discriminated direction/speed exclusively in the dark (vestibular only), or only when visual stimuli were available (vestibular + static visual only). Light blue indicates significant discrimination under both conditions.

(D) Summary data (median and 95% CI) showing percentage of cells that discriminated speed of rotation (10°/s v. 80°/s) under each condition. *p = 0.02, Wilcoxon signed rank test.

(E) Summary data (median and 95% CI) showing percentage of cells that discriminated direction of rotation under each condition, using either the first 500 ms (left) or the entire rotation window (right, 3.5 s). ***p = 3e−4, (ns) p = 0.73, Wilcoxon signed rank test.

decoding accuracy for the entire rotation window: vestibular = 95.8% ± 2.9%, vestibular + visual = 96.6% ± 2.5%, 5 pseudo-populations, 10–120 pooled neurons, p = 0.16, one-way ANOVA with Holm-Sidak's test; Figure 6C). This may be explained by the relatively slow processing time of vestibular compared to visual information (Barnett-Cowan and Harris, 2009) and the significance of multisensory integration in resolving ambiguities at the beginning of motion. Finally, we obtained similar results when using all populations of simultaneously recorded RSP neurons (Figure S8).

DISCUSSION

We have provided a quantitative analysis of sensory mechanisms underlying cortical AHV coding. Our results reveal a previously underappreciated extensive network of AHV-tuned cells in the RSP that is dominated by vestibular input and can reliably encode the direction and speed of head turns during both active exploration and passive motion. The AHV (and locomotion speed) cells in the RSP may be used in path integration by updating the spatial map as the animal moves through the environment, and possibly contribute to the perception of self-motion. These neurons may also engage in generation and updating of egocentric goal vector tuning in the RSP and downstream regions (Vale et al., 2020), as well as egocentric boundary vector tuning (Alexander et al., 2020; Laurens et al., 2019; van Wijngaarden et al., 2020) which is prevalent in this area. It is noteworthy that the experimental design employed here uses drop-off boundaries (instead of physical walls) and absence of objects or any specific goal in the open arena to purposefully reduce the involvement of these other cell types. Therefore, the interaction between RSP cells that encode self-motion and those that exhibit self-referenced tuning to spatial features remains an important open question.

By demonstrating the maintenance of AHV tuning between freely moving and head-restrained conditions in the large majority of RSP neurons (80%), we show that proprioceptive signals and efference copy of motor commands that arise from voluntary head movements and locomotion are not major drivers of retrosplenial AHV cells. Nevertheless, considering that a small number of AHV cells (18/90) did not show significant correlation with passive angular velocity and that tuning properties in half of AHV cells varied between the two conditions, motor-related signals may provide additional input to these neurons and modulate angular velocity coding during navigation. This interpretation is consistent with the existence of direct projections from motor cortices to the RSP (Oh et al., 2014; Shibata and Naito, 2008; Yamawaki et al., 2016) and also with the observation that many vestibular neurons in the brainstem integrate proprioceptive and motor related information (Medrea and Cullen, 2013). Alternatively, differences between active and passive AHV tuning may arise from cortical posture-related signals in freely moving animals (Mimica et al., 2018), and/or the substantially more complex head movements during free exploration which encompass

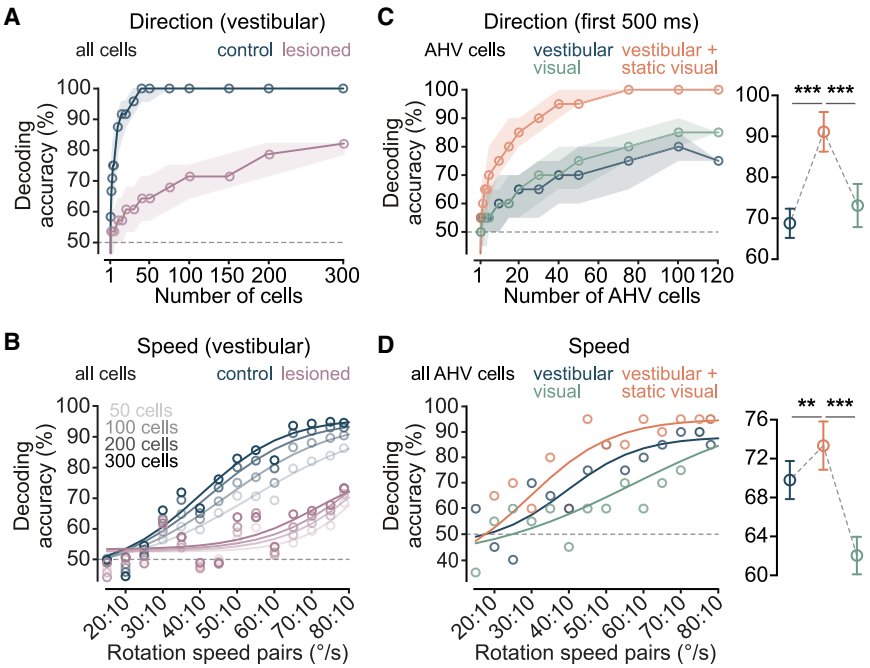

Figure 6. Combination of vestibular and visual stimuli improves decoding of angular self-motion by AHV cell populations

(A) LDA direction decoding accuracy (mean + IQR) in darkness as a function of population size for controls and vestibular-lesioned animals.

(B) LDA speed decoding accuracies (10°/s v. 15°/s – 80°/s) in darkness with increasing population size for controls and vestibular-lesioned animals.

(C) Left: LDA decoding accuracy (mean + IQR) for direction of self-rotation (blue and orange) and visual motion (green) as a function of AHV population size. Only the initial 500 ms of stimuli was considered. Right: mean (±SEM) decoding accuracy (5 pseudo-populations, 10 – 120 pooled neurons). ***p (vestibular v. vestibular + visual) = 4.2e-4, ***p (visual v. vestibular + visual) = 4.2e-4, one-way ANOVA with Holm-Sidak's test.

(D) Left: LDA decoding accuracies for speed of self-rotation (blue and orange) and visual motion (green) using all 120 AHV cells pooled into a pseudo-population. Lines are sigmoid fits. Right: mean (±SEM) decoding accuracy from all speed pairs (5 pseudo-populations, 10 – 120 pooled neurons). **p (vestibular v. vestibular + visual) = 0.007, ***p (visual v. vestibular + visual) = 0.0004, one-way ANOVA with Holm-Sidak's test. See also Figure S8.

multiple planes of motion in three-dimensional space, as opposed to exclusive horizontal rotations in our head-fixed experiments. In addition, considering that many RSP AHV cells are conjunctively tuned to linear speed and heading direction, modulation by these other navigational variables during free exploration may further contribute to AHV tuning differences between the two experimental setups. The absence of substantial eye movement-related activity in the RSP further suggests that eye-movement-sensitive neurons in the vestibular nuclei (Beraneck and Cullen, 2007), which are modulated by pupil position and the fast phase of VOR, are not the primary source of AHV tuning in the RSP. However, it is likely that brainstem neurons with integrated eye and head movement information further contribute to the ascending AHV signal (Cullen and Taube, 2017; Shinder and Taube, 2014).

The prevalence of AHV cells in the RSP and the large fraction of conjunctive head direction × AHV cells identified here is at odds with the current network model of the mammalian head direction system, which assumes that cortical areas such as the RSP inherit a pure allocentric heading representation from subcortical regions via the anterior thalamus (Peyrache et al., 2019; Taube, 2007). In this hierarchical model, AHV and conjunctive cells predominantly reside in brainstem nuclei. The head direction signal is then generated by integrating AHV over time in the tegmentomammillary circuit (Bassett et al., 2007) and passed along to higher thalamocortical areas. In contrast, our data suggest that the neural substrates required for generation and updating of the head direction signal, namely AHV and conjunctive head direction × AHV cells (Blair, 1995; Redish et al., 1996; Skaggs et al., 1995; Zhang, 1996), also exist in the cortex. Interestingly, the proportion of AHV-tuned neurons in the RSP and their tuning properties resembles those described in the brainstem dorsal tegmental nucleus (Bassett and Taube, 2001; Sharp et al., 2001), which is considered as the site of head direction signal generation. It is therefore likely that AHV neurons in the RSP also contribute to local generation of the cortical head direction signal. Although previous studies have shown that lesioning the anterodorsal thalamus (ADT) abolishes head direction cell activity in the postsubiculum (Goodridge and Taube, 1997) and entorhinal cortex (Winter et al., 2015), similar data in support of passive inheritance of head direction tuning in the RSP is lacking. Future work is thus required to establish whether both cortical and subcortical regions are involved in generating the head direction signal.

We have also shown that additional visual input to the RSP increases the gain and signal-to-noise ratio of individual AHV cells and the fidelity of encoding the direction and speed of head turns at the network level. This is in line with our behavioral data and previous work in primates (Butler et al., 2010; DeAngelis and Angelaki, 2012; Fetsch et al., 2011; Fetsch et al., 2009; Gu et al., 2008) showing improved perception of self-motion when visual cues are present. Therefore, while vestibular input appears to be critical for encoding cortical AHV, visual input has a gain-of-function role in self-motion signaling during navigation. The contribution of vision in this process may consist of the combined effect of optic-flow, which provides additional motion information, luminance (Bouvier et al., 2020), which can modulate AHV tuning, and the improved gain of gaze-stabilizing eye movements when VOR and optokinetic reflexes work together (Stahl, 2004). We thus propose that the significance of visual input to the RSP—and likely to other parts of the head direction network—extends beyond allocentric representation of spatial landmarks (Auger et al., 2012; Bicanski and Burgess, 2016; Fischer et al., 2020;

Jacob et al., 2017; Page and Jeffery, 2018). Instead, both external and self-generated visual information can be used to maintain accurate spatial orientation.

These data provide a mechanistic explanation of turn-specific modulations of neural activity during route running observed in the RSP (Alexander and Nitz, 2015) and beyond (McNaughton et al., 1994; Nitz, 2006; Whitlock et al., 2012). They also highlight a critical role of the vestibular sense in cortical processing, which despite its vital role in spatial cognition has received relatively little attention. The robust representation of vestibular stimuli observed here complements and extends recent work on vestibular-evoked responses in the rodent cortical network (Bouvier et al., 2020; Rancz et al., 2015; Vélez-Fort et al., 2018). AHV cells in the RSP may belong to the same population of cells that were previously shown to provide head motion information to the primary visual cortex (Vélez-Fort et al., 2018), and may also be the source of head motion signals in other cortical areas that are directly connected to the RSP, such as postsubiculum (Sharp, 1996) and entorhinal cortex (Mallory et al., 2021). In addition, these cells may engage in sensory-motor transformation during navigation via RSP projections to motor-related areas such as the secondary motor cortex (M2) and dorsal striatum (McGeorge and Faull, 1989; Yamawaki et al., 2016).

The pathways that provide AHV information to the RSP are yet to be described, but one possible route could involve the ascending thalamocortical head direction network via afferents from ADT. However, despite significant AHV tuning in upstream regions including the brainstem dorsal tegmental area (Bassett and Taube, 2001; Sharp et al., 2001) and lateral mammillary nucleus (Stackman and Taube, 1998), there is no evidence of substantial AHV coding in ADT (Bassett et al., 2007), and head direction cells in this area only show modest modulation by angular velocity (Blair and Sharp, 1995; Taube, 1995). Another route may involve projections from anteroventral and anteromedial thalamus. These thalamic areas receive direct input from the medial mammillary nucleus (Dillingham et al., 2021), which also contains large number of angular velocity coding cells (Sharp and Turner-Williams, 2005) and is connected to the vestibular system via the ventral tegmental area (Irle et al., 1984). Yet again, despite reports of head direction cells (Jankowski et al., 2015; Tsanov et al., 2011), AHV-tuned neurons have not been reported in these thalamic structures. Interestingly, recent modeling data suggest that synaptic dynamics of anterior thalamic inputs to the RSP may transform the head direction input to angular speed signal (Brennan et al., 2021). Alternatively, the laterodorsal thalamus, which receives direct afferents from the medial vestibular nucleus (Shiroyama et al., 1999) could be a source of AHV information. Finally, AHV signals may arise from posterior and ventral thalamic nuclei that are connected to the vestibular system (Wijesinghe et al., 2015) and reach the RSP via projections from other cortical regions such as the posterior parietal cortex where self-motion signals are widespread (Whitlock et al., 2012; Wilber et al., 2017).

Irrespective of the source of AHV inputs, there is a significant egocentric component to motion signaling in the RSP, indicating that this area can combine both environmental features (Alexander et al., 2020; Vale et al., 2020; van Wijngaarden et al., 2020) and correlates of movement into a coherent self-referenced spatial map.

STAR★METHODS

Detailed methods are provided in the online version of this paper and include the following:

- KEY RESOURCES TABLE
- RESOURCE AVAILABILITY
  - Lead contact
  - Materials availability
  - Data and code availability
- EXPERIMENTAL MODEL AND SUBJECT DETAILS
- METHOD DETAILS
  - Surgical procedures
  - Recording setups
- QUANTIFICATION AND STATISTICAL ANALYSIS
  - Open field analysis
  - Rotation analysis
  - ROC analysis
  - Population decoding
  - Statistics

SUPPLEMENTAL INFORMATION

Supplemental information can be found online at https://doi.org/10.1016/j.neuron.2021.10.031.

ACKNOWLEDGMENTS

We would like to thank Jasper Poort and Petr Znamenskiy for useful discussions. The authors are grateful to Charly Rousseau for his contribution to data acquisition/analysis pipelines and Gonçalo Lopes for the development of 3D visual stimulus presentation in Bonsai. We also thank Molly Strom, Rob Campbell, the SWC Neurobiological Research Facility, and FabLabs for technical support. This research was funded by the Sainsbury Wellcome Centre Core Grant from the Gatsby Charitable Foundation (GAT3361 to T.B. and T.W.M.) and Wellcome Trust (090843/F/09/Z to T.B. and T.W.M. and 214333/Z/18/Z to T.W.M.).

AUTHOR CONTRIBUTIONS

S.K. and T.W.M. conceived and led the project. S.K., E.B., and T.W.M. designed experiments. D.C. and T.B. designed and built the open field recording setup. E.F.B. performed the behavioral experiments. S.K. and E.F.B. analyzed the behavioral data. S.K. and D.C. performed the chronic probe implant surgeries. S.K. performed all other experiments and data analyses and designed the analysis of neural data. R.A.F. developed the "spikeGUI" analysis software. A.L.T. developed the "opendirection" analysis pipeline. S.C.L. and D.C. contributed to the development of data processing and analysis codes. T.B. and T.W.M. secured funding and resources. S.K. wrote the original draft. S.K. and T.W.M. revised and edited the manuscript with input from all the authors.

DECLARATION OF INTERESTS

The authors declare no competing interests.

Received: April 2, 2021
Revised: July 29, 2021
Accepted: October 20, 2021
Published: November 16, 2021

REFERENCES

Alexander, A.S., and Nitz, D.A. (2015). Retrosplenial cortex maps the conjunction of internal and external spaces. Nat. Neurosci. *18*, 1143–1151.

Alexander, A.S., and Nitz, D.A. (2017). Spatially Periodic Activation Patterns of Retrosplenial Cortex Encode Route Sub-spaces and Distance Traveled. Curr. Biol. *27*, 1551–1560.e4.

Alexander, A.S., Carstensen, L.C., Hinman, J.R., Raudies, F., Chapman, G.W., and Hasselmo, M.E. (2020). Egocentric boundary vector tuning of the retrosplenial cortex. Sci. Adv. *6*, eaaz2322.

Arenz, A., Silver, R.A., Schaefer, A.T., and Margrie, T.W. (2008). The contribution of single synapses to sensory representation in vivo. Science *321*, 977–980.

Auger, S.D., Mullally, S.L., and Maguire, E.A. (2012). Retrosplenial cortex codes for permanent landmarks. PLoS ONE *7*, e43620.

Barnett-Cowan, M., and Harris, L.R. (2009). Perceived timing of vestibular stimulation relative to touch, light and sound. Exp. Brain Res. *198*, 221–231.

Barthó, P., Hirase, H., Monconduit, L., Zugaro, M., Harris, K.D., and Buzsáki, G. (2004). Characterization of neocortical principal cells and interneurons by network interactions and extracellular features. J. Neurophysiol. *92*, 600–608.

Bassett, J.P., and Taube, J.S. (2001). Neural correlates for angular head velocity in the rat dorsal tegmental nucleus. J. Neurosci. *21*, 5740–5751.

Bassett, J.P., Tullman, M.L., and Taube, J.S. (2007). Lesions of the tegmentomammillary circuit in the head direction system disrupt the head direction signal in the anterior thalamus. J. Neurosci. *27*, 7564–7577.

Beraneck, M., and Cullen, K.E. (2007). Activity of vestibular nuclei neurons during vestibular and optokinetic stimulation in the alert mouse. J. Neurophysiol. *98*, 1549–1565.

Bicanski, A., and Burgess, N. (2016). Environmental Anchoring of Head Direction in a Computational Model of Retrosplenial Cortex. J. Neurosci. *36*, 11601–11618.

Blair, H.T. (1995). Simulation of a thalamocortical circuit for computing directional heading in the rat. Adv. Neural Inf. Process. Syst. *8*, 152–158.

Blair, H.T., and Sharp, P.E. (1995). Anticipatory head direction signals in anterior thalamus: evidence for a thalamocortical circuit that integrates angular head motion to compute head direction. J. Neurosci. *15*, 6260–6270.

Bouvier, G., Senzai, Y., and Scanziani, M. (2020). Head Movements Control the Activity of Primary Visual Cortex in a Luminance-Dependent Manner. Neuron *108*, 500–511.e5.

Brennan, E.K., Jedrasiak-Cape, I., Kailasa, S., Rice, S.P., Sudhakar, S.K., and Ahmed, O.J. (2021). Thalamus and claustrum control parallel layer 1 circuits in retrosplenial cortex. eLife *10*, e62207.

Butler, J.S., Smith, S.T., Campos, J.L., and Bülthoff, H.H. (2010). Bayesian integration of visual and vestibular signals for heading. J. Vis. *10*, 23.

Butler, W.N., Smith, K.S., van der Meer, M.A.A., and Taube, J.S. (2017). The Head-Direction Signal Plays a Functional Role as a Neural Compass during Navigation. Curr. Biol. *27*, 1259–1267.

Campbell, M.G., Ocko, S.A., Mallory, C.S., Low, I.I.C., Ganguli, S., and Giocomo, L.M. (2018). Principles governing the integration of landmark and self-motion cues in entorhinal cortical codes for navigation. Nat. Neurosci. *21*, 1096–1106.

Chen, L.L., Lin, L.-H., Barnes, C.A., and McNaughton, B.L. (1994a). Head-direction cells in the rat posterior cortex. II. Contributions of visual and ideothetic information to the directional firing. Exp. Brain Res. *101*, 24–34.

Chen, L.L., Lin, L.H., Green, E.J., Barnes, C.A., and McNaughton, B.L. (1994b). Head-direction cells in the rat posterior cortex. I. Anatomical distribution and behavioral modulation. Exp. Brain Res. *101*, 8–23.

Chinzorig, C., Nishimaru, H., Matsumoto, J., Takamura, Y., Berthoz, A., Ono, T., and Nishijo, H. (2020). Rat Retrosplenial Cortical Involvement in Wayfinding Using Visual and Locomotor Cues. Cereb. Cortex *30*, 1985–2004.

Cho, J., and Sharp, P.E. (2001). Head direction, place, and movement correlates for cells in the rat retrosplenial cortex. Behav. Neurosci. *115*, 3–25.

Chrastil, E.R., Sherrill, K.R., Hasselmo, M.E., and Stern, C.E. (2015). There and back again: Hippocampus and retrosplenial cortex track homing distance during human path integration. J. Neurosci. *35*, 15442–15452.

Chrastil, E.R., Sherrill, K.R., Aselcioglu, I., Hasselmo, M.E., and Stern, C.E. (2017). Individual differences in human path integration abilities correlate with gray matter volume in retrosplenial cortex, hippocampus, and medial prefrontal cortex. eNeuro *4*, 346–362.

Cooper, B.G., and Mizumori, S.J.Y. (1999). Retrosplenial cortex inactivation selectively impairs navigation in darkness. Neuroreport *10*, 625–630.

Cooper, B.G., and Mizumori, S.J.Y. (2001). Temporary inactivation of the retrosplenial cortex causes a transient reorganization of spatial coding in the hippocampus. J. Neurosci. *21*, 3986–4001.

Cooper, B.G., Manka, T.F., and Mizumori, S.J.Y. (2001). Finding your way in the dark: the retrosplenial cortex contributes to spatial memory and navigation without visual cues. Behav. Neurosci. *115*, 1012–1028.

Cullen, K.E. (2014). The neural encoding of self-generated and externally applied movement: implications for the perception of self-motion and spatial memory. Front. Integr. Nuerosci. *7*, 108.

Cullen, K.E., and Taube, J.S. (2017). Our sense of direction: progress, controversies and challenges. Nat. Neurosci. *20*, 1465–1473.

DeAngelis, G.C., and Angelaki, D.E. (2012). Visual-Vestibular Integration for Self-Motion Perception. In The Neural Bases of Multisensory Processes, M.M. Murray and M.T. Wallace, eds. (CRC Press/Taylor & Francis).

DeLong, E.R., DeLong, D.M., and Clarke-Pearson, D.L. (1988). Comparing the areas under two or more correlated receiver operating characteristic curves: a nonparametric approach. Biometrics *44*, 837–845.

Dillingham, C.M., Milczarek, M.M., Perry, J.C., and Vann, S.D. (2021). Time to put the mammillothalamic pathway into context. Neurosci. Biobehav. Rev. *121*, 60–74.

Elduayen, C., and Save, E. (2014). The retrosplenial cortex is necessary for path integration in the dark. Behav. Brain Res. *272*, 303–307.

Fetsch, C.R., Turner, A.H., DeAngelis, G.C., and Angelaki, D.E. (2009). Dynamic reweighting of visual and vestibular cues during self-motion perception. J. Neurosci. *29*, 15601–15612.

Fetsch, C.R., Pouget, A., DeAngelis, G.C., and Angelaki, D.E. (2011). Neural correlates of reliability-based cue weighting during multisensory integration. Nat. Neurosci. *15*, 146–154.

Fischer, L.F., Mojica Soto-Albors, R., Buck, F., and Harnett, M.T. (2020). Representation of visual landmarks in retrosplenial cortex. eLife *9*, e51458.

Frohardt, R.J., Bassett, J.P., and Taube, J.S. (2006). Path integration and lesions within the head direction cell circuit: comparison between the roles of the anterodorsal thalamus and dorsal tegmental nucleus. Behav. Neurosci. *120*, 135–149.

Giocomo, L.M., Stensola, T., Bonnevie, T., Van Cauter, T., Moser, M.B., and Moser, E.I. (2014). Topography of head direction cells in medial entorhinal cortex. Curr. Biol. *24*, 252–262.

Goodridge, J.P., and Taube, J.S. (1995). Preferential use of the landmark navigational system by head direction cells in rats. Behav. Neurosci. *109*, 49–61.

Goodridge, J.P., and Taube, J.S. (1997). Interaction between the postsubiculum and anterior thalamus in the generation of head direction cell activity. J. Neurosci. *17*, 9315–9330.

Green, J., Adachi, A., Shah, K.K., Hirokawa, J.D., Magani, P.S., and Maimon, G. (2017). A neural circuit architecture for angular integration in Drosophila. Nature *546*, 101–106.

Gu, Y., Angelaki, D.E., and Deangelis, G.C. (2008). Neural correlates of multisensory cue integration in macaque MSTd. Nat. Neurosci. *11*, 1201–1210.

Harris, C.R., Millman, K.J., van der Walt, S.J., Gommers, R., Virtanen, P., Cournapeau, D., Wieser, E., Taylor, J., Berg, S., Smith, N.J., et al. (2020). Array programming with NumPy. Nature *585*, 357–362.

Hunter, J.D. (2007). Matplotlib: a 2D Graphics Environment. Comput. Sci. Eng. *9*, 90–95.

Irle, E., Sarter, M., Guldin, W.O., and Markowitsch, H.J. (1984). Afferents to the ventral tegmental nucleus of Gudden in the mouse, rat, and cat. J. Comp. Neurol. *228*, 509–541.

Jacob, P.Y., Casali, G., Spieser, L., Page, H., Overington, D., and Jeffery, K. (2017). An independent, landmark-dominated head-direction signal in dysgranular retrosplenial cortex. Nat. Neurosci. *20*, 173–175.

Jankowski, M.M., Passecker, J., Islam, M.N., Vann, S., Erichsen, J.T., Aggleton, J.P., and O'Mara, S.M. (2015). Evidence for spatially-responsive neurons in the rostral thalamus. Front. Behav. Neurosci. *9*, 256.

Jun, J.J., Steinmetz, N.A., Siegle, J.H., Denman, D.J., Bauza, M., Barbarits, B., Lee, A.K., Anastassiou, C.A., Andrei, A., Aydın, Ç., et al. (2017). Fully integrated silicon probes for high-density recording of neural activity. Nature *551*, 232–236.

Jürgens, R., and Becker, W. (2006). Perception of angular displacement without landmarks: evidence for Bayesian fusion of vestibular, optokinetic, podokinesthetic, and cognitive information. Exp. Brain Res. *174*, 528–543.

Kropff, E., Carmichael, J.E., Moser, M.B., and Moser, E.I. (2015). Speed cells in the medial entorhinal cortex. Nature *523*, 419–424.

Laurens, J., and Angelaki, D.E. (2018). The Brain Compass: A Perspective on How Self-Motion Updates the Head Direction Cell Attractor. Neuron *97*, 275–289.

Laurens, J., Abrego, A., Cham, H., Popeney, B., Yu, Y., Rotem, N., Aarse, J., Asprodini, E.K., Dickman, J.D., and Angelaki, D.E. (2019). Multiplexed code of navigation variables in anterior limbic areas. bioRxiv, doi.org/10.1101/684464.

Lopes, G., Bonacchi, N., Frazão, J., Neto, J.P., Atallah, B.V., Soares, S., Moreira, L., Matias, S., Itskov, P.M., Correia, P.A., et al. (2015). Bonsai: an event-based framework for processing and controlling data streams. Front. Neuroinform. *9*, 7.

Maguire, E.A. (2001). The retrosplenial contribution to human navigation: a review of lesion and neuroimaging findings. Scand. J. Psychol. *42*, 225–238.

Mallory, C.S., Hardcastle, K., Campbell, M.G., Attinger, A., Low, I.I.C., Raymond, J.L., and Giocomo, L.M. (2021). Mouse entorhinal cortex encodes a diverse repertoire of self-motion signals. Nat. Commun. *12*, 671.

Mao, D., Kandler, S., McNaughton, B.L., and Bonin, V. (2017). Sparse orthogonal population representation of spatial context in the retrosplenial cortex. Nat. Commun. *8*, 243.

Mao, D., Molina, L.A., Bonin, V., and McNaughton, B.L. (2020). Vision and Locomotion Combine to Drive Path Integration Sequences in Mouse Retrosplenial Cortex. Curr. Biol. *30*, 1680–1688..

Mathis, A., Mamidanna, P., Cury, K.M., Abe, T., Murthy, V.N., Mathis, M.W., and Bethge, M. (2018). DeepLabCut: markerless pose estimation of user-defined body parts with deep learning. Nat. Neurosci. *21*, 1281–1289.

McGeorge, A.J., and Faull, R.L. (1989). The organization of the projection from the cerebral cortex to the striatum in the rat. Neuroscience *29*, 503–537.

McNaughton, B.L., Chen, L.L., and Markus, E.J. (1991). "Dead reckoning," landmark learning, and the sense of direction: a neurophysiological and computational hypothesis. J. Cogn. Neurosci. *3*, 190–202.

McNaughton, B.L., Mizumori, S.J.Y., Barnes, C.A., Leonard, B.J., Marquis, M., and Green, E.J. (1994). Cortical representation of motion during unrestrained spatial navigation in the rat. Cereb. Cortex *4*, 27–39.

McNaughton, B.L., Knierim, J.J., and Wilson, M.A. (1995). Vector Encoding and the Vestibular Foundations of Spatial Cognition: Neurophysiological and Computational Mechanisms. In The Cognitive Neurosciences, M.S. Gazzaniga, ed. (The MIT Press), pp. 585–595.

Medrea, I., and Cullen, K.E. (2013). Multisensory integration in early vestibular processing in mice: the encoding of passive vs. active motion. J. Neurophysiol. *110*, 2704–2717.

Mimica, B., Dunn, B.A., Tombaz, T., Bojja, V.P.T., and Whitlock, J.R. (2018). Efficient cortical coding of 3D posture in freely behaving rats. Science *362*, 584–589.

Muir, G.M., Brown, J.E., Carey, J.P., Hirvonen, T.P., Della Santina, C.C., Minor, L.B., and Taube, J.S. (2009). Disruption of the head direction cell signal after occlusion of the semicircular canals in the freely moving chinchilla. J. Neurosci. *29*, 14521–14533.

Niedworok, C.J., Brown, A.P., Jorge Cardoso, M., Osten, P., Ourselin, S., Modat, M., and Margrie, T.W. (2016). aMAP is a validated pipeline for registration and segmentation of high-resolution mouse brain data. Nat. Commun. *7*, 11879.

Nitz, D.A. (2006). Tracking route progression in the posterior parietal cortex. Neuron *49*, 747–756.

Oh, S.W., Harris, J.A., Ng, L., Winslow, B., Cain, N., Mihalas, S., Wang, Q., Lau, C., Kuan, L., Henry, A.M., et al. (2014). A mesoscale connectome of the mouse brain. Nature *508*, 207–214.

Pachitariu, M., Steinmetz, N., Kadir, S., Carandini, M., and Harris, K.D. (2016). Fast and accurate spike sorting of high-channel count probes with KiloSort, , 30th Conference on Neural Information Processing. In Advances in Neural Information Processing 29 (NIPS 2016), D. Lee, M. Sugiyama, U. Luxburg, I. Guyon, and R. Garnett, eds. (NeurIPS Proceedings).

Page, H.J.I., and Jeffery, K.J. (2018). Landmark-Based Updating of the Head Direction System by Retrosplenial Cortex: A Computational Model. Front. Cell. Neurosci. *12*, 191.

Pedregosa, F., Varoquaux, G., Gramfort, A., Michel, V., Thirion, B., Grisel, O., Blondel, M., Prettenhofer, P., Weiss, R., Dubourg, V., et al. (2011). Scikit-learn: Machine Learning in Python. J. Mach. Learn. Res. *12*, 2825–2830.

Peyrache, A., Duszkiewicz, A.J., Viejo, G., and Angeles-Duran, S. (2019). Thalamocortical processing of the head-direction sense. Prog. Neurobiol. *183*, 101693.

Powell, A., Connelly, W.M., Vasalauskaite, A., Nelson, A.J.D., Vann, S.D., Aggleton, J.P., Sengpiel, F., and Ranson, A. (2020). Stable Encoding of Visual Cues in the Mouse Retrosplenial Cortex. Cereb. Cortex *30*, 4424–4437.

Preston-Ferrer, P., Coletta, S., Frey, M., and Burgalossi, A. (2016). Anatomical organization of presubicular head-direction circuits. eLife *5*, 1–20.

Prsa, M., Gale, S., and Blanke, O. (2012). Self-motion leads to mandatory cue fusion across sensory modalities. J. Neurophysiol. *108*, 2282–2291.

Rancz, E.A., Moya, J., Drawitsch, F., Brichta, A.M., Canals, S., and Margrie, T.W. (2015). Widespread vestibular activation of the rodent cortex. J. Neurosci. *35*, 5926–5934.

Ravassard, P., Kees, A., Willers, B., Ho, D., Aharoni, D.A., Cushman, J., Aghajan, Z.M., and Mehta, M.R. (2013). Multisensory control of hippocampal spatiotemporal selectivity. Science *340*, 1342–1346.

Reback, J., McKinney, W., jbrockmendel, Van den Bossche, J., Augspurger, T., Cloud, P., gfyoung, Sinhrks, Klein, A., Roeschke, M., et al. (2020). pandas-dev/pandas: Pandas 1.0.3. https://doi.org/10.5281/zenodo.3715232.

Redish, D., Elga, A.N., and Touretzky, D.S. (1996). A coupled attractor model of the rodent head direction system. Network: Comput. in Neural Syst. *7*, 671–685.

Robertson, R.G., Rolls, E.T., Georges-François, P., and Panzeri, S. (1999). Head direction cells in the primate pre-subiculum. Hippocampus *9*, 206–219.

Robin, X., Turck, N., Hainard, A., Tiberti, N., Lisacek, F., Sanchez, J.C., and Müller, M. (2011). pROC: an open-source package for R and S+ to analyze and compare ROC curves. BMC Bioinformatics *12*, 77.

Rothman, J.S., and Silver, R.A. (2018). NeuroMatic: An Integrated Open-Source Software Toolkit for Acquisition, Analysis and Simulation of Electrophysiological Data. Front. Neuroinform. *12*, 14.

Salvador, S., and Chan, P. (2007). FastDTW: Toward Accurate Dynamic Time Warping in Linear Time and Space. Intell. Data Anal. *11*, 561–580.

Schindelin, J., Arganda-Carreras, I., Frise, E., Kaynig, V., Longair, M., Pietzsch, T., Preibisch, S., Rueden, C., Saalfeld, S., Schmid, B., et al. (2012). Fiji: an open-source platform for biological-image analysis. Nat. Methods *9*, 676–682.

Seelig, J.D., and Jayaraman, V. (2015). Neural dynamics for landmark orientation and angular path integration. Nature *521*, 186–191.

Sharp, P.E. (1996). Multiple spatial/behavioral correlates for cells in the rat postsubiculum: multiple regression analysis and comparison to other hippocampal areas. Cereb. Cortex *6*, 238–259.

Sharp, P.E., and Turner-Williams, S. (2005). Movement-related correlates of single-cell activity in the medial mammillary nucleus of the rat during a pellet-chasing task. J. Neurophysiol. *94*, 1920–1927.

Sharp, P.E., Tinkelman, A., and Cho, J. (2001). Angular velocity and head direction signals recorded from the dorsal tegmental nucleus of gudden in the rat: implications for path integration in the head direction cell circuit. Behav. Neurosci. *115*, 571–588.

Shibata, H., and Naito, J. (2008). Organization of anterior cingulate and frontal cortical projections to the retrosplenial cortex in the rat. J. Comp. Neurol. *506*, 30–45.

Shinder, M.E., and Taube, J.S. (2011). Active and passive movement are encoded equally by head direction cells in the anterodorsal thalamus. J. Neurophysiol. *106*, 788–800.

Shinder, M.E., and Taube, J.S. (2014). Resolving the active versus passive conundrum for head direction cells. Neuroscience *270*, 123–138.

Shiroyama, T., Kayahara, T., Yasui, Y., Nomura, J., and Nakano, K. (1999). Projections of the vestibular nuclei to the thalamus in the rat: a Phaseolus vulgaris leucoagglutinin study. J. Comp. Neurol. *407*, 318–332.

Skaggs, W.E., Knierim, J.J., Kudrimoti, H.S., and McNaughton, B.L. (1995). A model of the neural basis of the rat's sense of direction. Adv. Neural Inf. Process. Syst. *7*, 173–180.

Stackman, R.W., and Taube, J.S. (1998). Firing properties of rat lateral mammillary single units: head direction, head pitch, and angular head velocity. J. Neurosci. *18*, 9020–9037.

Stahl, J.S. (2004). Using eye movements to assess brain function in mice. Vision Res. *44*, 3401–3410.

Steinmetz, N.A., Aydin, C., Lebedeva, A., Okun, M., Pachitariu, M., Bauza, M., Beau, M., Bhagat, J., Böhm, C., Broux, M., et al. (2021). Neuropixels 2.0: A miniaturized high-density probe for stable, long-term brain recordings. Science *372*. https://doi.org/10.1126/science.abf4588.

Takahashi, N., Kawamura, M., Shiota, J., Kasahata, N., and Hirayama, K. (1997). Pure topographic disorientation due to right retrosplenial lesion. Neurology *49*, 464–469.

Taube, J.S. (1995). Head direction cells recorded in the anterior thalamic nuclei of freely moving rats. J. Neurosci. *15*, 70–86.

Taube, J.S. (2007). The head direction signal: origins and sensory-motor integration. Annu. Rev. Neurosci. *30*, 181–207.

Taube, J.S., Muller, R.U., and Ranck, J.B., Jr. (1990a). Head-direction cells recorded from the postsubiculum in freely moving rats. I. Description and quantitative analysis. J. Neurosci. *10*, 420–435.

Taube, J.S., Muller, R.U., and Ranck, J.B., Jr. (1990b). Head-direction cells recorded from the postsubiculum in freely moving rats. II. Effects of environmental manipulations. J. Neurosci. *10*, 436–447.

Tsanov, M., Chah, E., Vann, S.D., Reilly, R.B., Erichsen, J.T., Aggleton, J.P., and O'Mara, S.M. (2011). Theta-modulated head direction cells in the rat anterior thalamus. J. Neurosci. *31*, 9489–9502.

Turner-Evans, D., Wegener, S., Rouault, H., Franconville, R., Wolff, T., Seelig, J.D., Druckmann, S., and Jayaraman, V. (2017). Angular velocity integration in a fly heading circuit. eLife *6*, e23496.

Tyson, A.L., Rousseau, C.V., Niedworok, C.J., Keshavarzi, S., Tsitoura, C., Cossell, L., Strom, M., and Margrie, T.W. (2021). A deep learning algorithm for 3D cell detection in whole mouse brain image datasets. PLoS Comput. Biol. *17*, e1009074.

Vale, R., Campagner, D., Iordanidou, P., Arocas, O.P., Tan, Y.L., Stempel, A.V., Keshavarzi, S.S., Petersen, R., Margrie, T., and Branco, T. (2020). A cortico-collicular circuit for accurate orientation to shelter during escape. bioRxiv. https://doi.org/10.1101/2020.05.26.117598.

van Groen, T., and Wyss, J.M. (1990). Connections of the retrosplenial granular a cortex in the rat. J. Comp. Neurol. *300*, 593–606.

van Groen, T., and Wyss, J.M. (1992). Connections of the retrosplenial dysgranular cortex in the rat. J. Comp. Neurol. *315*, 200–216.

van Wijngaarden, J.B., Babl, S.S., and Ito, H.T. (2020). Entorhinal-retrosplenial circuits for allocentric-egocentric transformation of boundary coding. eLife *9*, e59816.

Vann, S.D., Aggleton, J.P., and Maguire, E.A. (2009). What does the retrosplenial cortex do? Nat. Rev. Neurosci. *10*, 792–802.

Vedder, L.C., Miller, A.M.P., Harrison, M.B., and Smith, D.M. (2017). Retrosplenial Cortical Neurons Encode Navigational Cues, Trajectories and Reward Locations During Goal Directed Navigation. Cereb. Cortex *27*, 3713–3723.

Vélez-Fort, M., Bracey, E.F., Keshavarzi, S., Rousseau, C.V., Cossell, L., Lenzi, S.C., Strom, M., and Margrie, T.W. (2018). A Circuit for Integration of Head- and Visual-Motion Signals in Layer 6 of Mouse Primary Visual Cortex. Neuron *98*, 179–191.e6.

Virtanen, P., Gommers, R., Oliphant, T.E., Haberland, M., Reddy, T., Cournapeau, D., Burovski, E., Peterson, P., Weckesser, W., Bright, J., et al.; SciPy 1.0 Contributors (2020). SciPy 1.0: fundamental algorithms for scientific computing in Python. Nat. Methods *17*, 261–272.

Wallace, D.G., Hines, D.J., Pellis, S.M., and Whishaw, I.Q. (2002). Vestibular information is required for dead reckoning in the rat. J. Neurosci. *22*, 10009–10017.

Wang, Q., Ding, S.L., Li, Y., Royall, J., Feng, D., Lesnar, P., Graddis, N., Naeemi, M., Facer, B., Ho, A., et al. (2020). The Allen Mouse Brain Common Coordinate Framework: A 3D Reference Atlas. Cell *181*, 936–953.e20.

Waskom, M., Gelbart, M., Botvinnik, O., Ostblom, J., Hobson, P., Lukauskas, S., Gemperline, D.C., Augspurger, T., Halchenko, Y., Warmenhoven, J., et al. (2020). mwaskom/seaborn, v0.11.1 g/10.5281/zenodo.4379347.

Whishaw, I.Q., Maaswinkel, H., Gonzalez, C.L.R., and Kolb, B. (2001). Deficits in allothetic and idiothetic spatial behavior in rats with posterior cingulate cortex lesions. Behav. Brain Res. *118*, 67–76.

Whitlock, J.R., Pfuhl, G., Dagslott, N., Moser, M.B., and Moser, E.I. (2012). Functional split between parietal and entorhinal cortices in the rat. Neuron *73*, 789–802.

Wijesinghe, R., Protti, D.A., and Camp, A.J. (2015). Vestibular Interactions in the Thalamus. Front. Neural Circuits *9*. https://doi.org/10.3389/fncir.2015.00079.

Wilber, A.A., Skelin, I., Wu, W., and McNaughton, B.L. (2017). Laminar Organization of Encoding and Memory Reactivation in the Parietal Cortex. Neuron *95*, 1406–1419.e5.

Winter, S.S., Clark, B.J., and Taube, J.S. (2015). Spatial navigation. Disruption of the head direction cell network impairs the parahippocampal grid cell signal. Science *347*, 870–874.

Yamawaki, N., Radulovic, J., and Shepherd, G.M.G. (2016). A Corticocortical Circuit Directly Links Retrosplenial Cortex to M2 in the Mouse. J. Neurosci. *36*, 9365–9374.

Yartsev, M.M., Witter, M.P., and Ulanovsky, N. (2011). Grid cells without theta oscillations in the entorhinal cortex of bats. Nature *479*, 103–107.

Yoder, R.M., Peck, J.R., and Taube, J.S. (2015). Visual landmark information gains control of the head direction signal at the lateral mammillary nuclei. J. Neurosci. *35*, 1354–1367.

Zhang, K. (1996). Representation of spatial orientation by the intrinsic dynamics of the head-direction cell ensemble: a theory. J. Neurosci. *16*, 2112–2126.

Zugaro, M.B., Arleo, A., Berthoz, A., and Wiener, S.I. (2003). Rapid spatial reorientation and head direction cells. J. Neurosci. *23*, 3478–3482.

STAR★METHODS

KEY RESOURCES TABLE

Reagent or resource	Source	Identifier
Experimental models: Organisms/strains		
Mouse: male C57BL/6	Charles River Laboratories	N/A
Chemicals, peptides, and recombinant proteins		
Isoflurane (IsoFlo)	Zoetis	N/A
Fentanyl	Martindale Pharma	N/A
Medetomidin (Medetor)	Chanelle Pharma	N/A
Midazolam (Hypnovel)	Roche	N/A
Naloxone	Mercury Pharma	N/A
Flumazenil	Teva UK	N/A
Atipamezole (Atipam)	Eurovet	N/A
Carprofen (Carprieve)	Norbrook	NA
Meloxicam (Metacam)	Boehringer Ingelheim Animal Health	N/A
Pentobarbital (Euthatal)	Merial Animal Health	N/A
Kanamycin sulfate	Generon	Cat# 41110000-6
Lubrithal eye gel	Dechra	N/A
Histoacryl tissue adhesive	Braun Medical	N/A
DiI	Thermo Fisher - Molecular Probes	Cat# V22885
DAPI	Santa Cruz Biotechnology	CAS 28718-90-3
Simplex Rapid dental cement (powder and liquid)	Kemdent	N/A
Kwik-Cast silicone sealant	World Precision Instrument	N/A
Resin dental cement (RelyX)	3M	Cat# 56846
Super-Bond C&B	Sun Medical	N/A
Tergazyme	Alconox	Cat# 1304-1
Software and algorithms		
aMAP	Niedworok et al., 2016	https://github.com/SainsburyWellcomeCentre/aMAP
Cellfinder	Tyson et al., 2021	doi.org/10.5281/zenodo.3891338; https://github.com/brainglobe/cellfinder
Kilosort	Pachitariu et al., 2016	https://github.com/cortex-lab/KiloSort
Phy	N/A	https://github.com/cortex-lab/phy
Python 3	https://www.python.org/	RRID: SCR_008394
DeepLabCut	Mathis et al., 2018	https://github.com/DeepLabCut/DeepLabCut
Kilosort2	Steinmetz et al., 2021	https://doi.org/10.5281/zenodo.4147288 https://github.com/MouseLand/Kilosort
SpikeGLX	Janelia Research Campus	https://github.com/billkarsh/SpikeGLX
Pyper	Vélez-Fort et al., 2018	https://github.com/SainsburyWellcomeCentre/Pyper
opendirection	https://github.com/adamltyson/opendirection	https://doi.org/10.5281/zenodo.5573967
spikeGUI	https://github.com/RichardFav/spikeGUI	https://doi.org/10.5281/zenodo.5574028
Neuromatic	Rothman and Silver, 2018	RRID:SCR_004186; http://www.neuromatic.thinkrandom.com/
Igor Pro	WaveMetrics	RRID:SCR_000325; https://www.wavemetrics.com/products/igorpro/igorpro.htm

(*Continued on next page*)

Continued

Reagent or resource	Source	Identifier
Bonsai	Lopes et al., 2015	https://open-ephys.org/bonsai
Mantis Software	Mantis	mantis64.com
MATLAB	MathWorks	RRID: SCR_001622; https://www.mathworks.com/products/matlab.html
FIJI	NIH; Schindelin et al., 2012	RRID:SCR_002285; https://imagej.net/Fiji
OpenCV	https://opencv.org/	RRID: SCR_001905
R	http://www.r-project.org/	RRID: SCR_001905
Scikit-learn	Pedregosa et al., 2011	RRID:SCR_002577; https://github.com/scikitlearn/scikit-learn
fastdtw package	Salvador and Chan, 2007	https://github.com/slaypni/fastdtw
pycircstat		https://github.com/circstat/pycircstat
pROC package of R	Robin et al., 2011	https://www.expasy.org/resources/proc
Numpy	Harris et al., 2020	RRID:SCR_008633; https://github.com/numpy/numpy
Scipy	Virtanen et al., 2020	RRID:SCR_008058; https://github.com/scipy/scipy
Pandas	Reback et al., 2020	https://doi.org/10.5281/zenodo.3715232 https://github.com/pandas-dev/pandas
matplotlib	Hunter, 2007	RRID:SCR_008624; https://github.com/matplotlib/matplotlib
LabVIEW	National Instruments	RRID:SCR_014325; https://www.ni.com/labview/
Allen Common Coordinate Framework	Allen Institute for Brain Science, Wang et al., 2020	RRID:SCR_005984; http://atlas.brain-map.org/

RESOURCE AVAILABILITY

Lead contact

Further requests for resources and reagents should be directed to Troy Margrie (t.margrie@ucl.ac.uk)

Materials availability

This study did not generate new unique reagents.

Data and code availability

- All raw data will be made available upon request from the lead contact.
- Original code (spikeGUI and opendirection) has been deposited at Zenodo and is publicly available as of the date of publication. DOIs are referenced in the Key Resources Table.
- Any additional information required to reanalyze the data reported in this paper is available from the lead contact upon request.

EXPERIMENTAL MODEL AND SUBJECT DETAILS

A total of 18 adult (8 – 14 weeks old, 25–35 g) male C57BL/6 mice were used in accordance with the regulations of the United Kingdom Home Office and the local Animal Welfare and Ethical Review Body (AWERB). Mice were maintained on a 12-hr reversed light/dark cycle and single housed after surgical procedures.

METHOD DETAILS

Surgical procedures

All surgical procedures were carried out under anesthesia either with isoflurane (2% – 5%) or with a mixture of fentanyl (0.05 mg/kg), midazolam (5.0 mg/kg), and medetomidine (0.5 mg/kg) in saline solution (0.9%, i.p.). Mice were then fixed in a stereotaxic frame and eyes were protected with a lubricating eye gel (Lubrithal, Dechra). Body temperature (37 – 38°C) and anesthesia level was maintained throughout the procedure. Carprofen (5 mg/kg, s.c.) or Meloxicam (1-2 mg/kg, s.c.) was administered for postoperative analgesia and, where appropriate, injectable anesthetics were reversed with a mixture of naloxone (1.2 mg/kg), flumazenil (0.5 mg/kg) and atipamezole (2.5 mg/kg) in saline solution (0.9%, i.p.).

For probe recordings, a custom-built titanium head fixation implant was affixed to the skull using a cyanoacrylate-based adhesive (Histoacryl, Braun Medical) and dental cement (Simplex Rapid, Kemdent and Super-Bond C&B, Sun Medical). A 1 mm craniotomy was performed with a 0.3 mm burr dental drill (Osada Electric, Japan) over the right RSP (AP: −3.40 to −2.20 mm, ML: 0.55 to 1.10 mm). For acute recordings, the craniotomy was performed 3 – 24 hours in advance and sealed with a removable silicone sealant (Kwik-Cast, World Precision Instrument). Chronic probe implants were fixed to the skull using a light-cured resin dental cement (3M, Relyx Unicem 2). In addition, a gold pin was inserted inside a craniotomy rostral to the Bregma, secured to the skull, and attached to the ground wire. Neuropixels implants were additionally secured inside a custom-built 3D printed enclosure (Vale et al., 2020).

For bilateral vestibular lesions, an incision was made behind each ear and muscles covering the temporal bone were bluntly dissected to expose the posterior and horizontal semi-circular canals. Canal bones were then thinned with a 0.3 mm burr dental drill until punctured and a microfiber needle was inserted into each canal to deliver 50 μL of kanamycin (50 mg/ml) in distilled water. After approximately 5 minutes, the solution was removed with a sterile cotton tip and the wound was closed using a cyanoacrylate-based adhesive.

Recording setups

Open field experiments

Open field recordings were performed on an elevated 92-cm diameter circular arena located inside a 140 × 140 × 160 cm sound-proof enclosure (Vale et al., 2020). A surrounding hectagonal black wall (45 cm high from the arena surface) was placed at approximately 10-cm distance from its circumference. Six infrared LEDs (TV6700, Abus) were positioned on enclosure walls to provide illumination. Mice were allowed to freely explore while their behavior was monitored at 40 frames per second (fps) with a near-IR camera (acA1300-60 gmNIR, Basler) centered above the arena. During light conditions, the background luminance was set at 11.5 lux using a projector (BenQ MW843UST) pointing at a translucent overhead screen (Xerox). Video recordings were controlled by a custom software written in LabVIEW (2015 64-bit, National Instruments) and Mantis software (mantis64.com). A PCIe-6351 board (National Instruments) was used to control triggering of each camera frame and for synchronization. A Neuronexus commutator or a custom-made rotary joint (adapted from Doric AHRJ-OE_PT_AH_12_HDMI) was used to prevent twisting of probe cables during recording. To correct for any potential drift between camera triggers and probe recording, a microcontroller (Arduino Leonardo) was used to continuously deliver logic pulses of varying time durations (randomly sampled from a uniform distribution).

All open field sessions consisted of three experimental conditions, each lasting 20 – 30 minutes. Recordings were first made in light (light1) where two side-by-side white cue cards (88 × 60 cm) were attached inside of the otherwise featureless black wall. Further recordings were made in darkness, and again in a second identical light condition (light2). At the completion of each open field recording session, mice were taken to the head-restrained passive rotation apparatus. The two recordings always occurred on the same day with a maximum of 5 hours in between.

Passive rotation experiments

Mice were head-fixed and restrained in a custom-made tube mounted onto a recording platform that was attached to the rotation motor (RV120CC, Newport Corporation). The animal's head was positioned such that the axis joining the ears was parallel to the horizontal plane of motion, with vestibular apparatuses positioned around the axis of rotation (Arenz et al., 2008; Vélez-Fort et al., 2018). Prior to recordings, mice were habituated to head fixation and rotation for 2 – 3 days with each habituation session lasting 15 – 30 minutes. Throughout habituation mice were given a sweetened condensed milk reward.

Visual stimuli were presented with a custom-built 3D surround projection system made of two laser projectors (MP-CL1A, Sony) and a cylindrical rear-projection screen (radius = 10 cm, height = 15 cm, central angle = 300°). The cylindrical screen was positioned concentrically with the rotation motor such that the animal's head was positioned at its center. Control of visual stimuli, alignment of images from the two projectors, image warping, edge blending and luminance correction were all implemented using custom algorithms written in Bonsai (Lopes et al., 2015). The animal's field of view was restricted with a pair of blinkers (azimuth = 120°, altitude = 50°) to prevent viewing beyond the screen boundaries during rotation. The visual stimulus consisted of either stationary or rotating full-field vertical square-wave gratings, with a mean luminance of 16 lux and a spatial frequency of 0.04 cpd. Horizontal rotation of the recording platform, or the vertical grating, was achieved using custom-written routines in Igor Pro in combination with NeuroMatic (Rothman and Silver, 2018). Rotation stimulus consisted of a full sinusoidal period (7 s), flanked by sinusoidal ramps of the same period, and reached a maximum displacement of 90° and a maximum velocity of 80°/s in each direction (CW or CCW, Figure 2A). Each rotation stimulus was separated by a stationary period (10 – 30 s) and repeated 10 – 15 times under each experimental condition. Waveforms used to rotate the platform and the surround visual stimulus were identical. To block any spatial auditory cues from the rotation motor or the environment, a masking white noise was played throughout the recording using a piezoelectric miniature speaker (Sonitron) mounted behind the animal on the platform. Synchronization with the probe recording was achieved by logic signals via an ITC-18 board (InstruTECH, Heka Elektronik). In addition, a photodiode (PDA100A-EC, Thorlab), placed out of the field of view behind the projection screen, was used to precisely record the onset of visual stimuli.

Each recording session consisted of three experimental conditions (Figure 4B): 1) rotation of the mouse in complete darkness ("vestibular"), 2) rotation of the mouse in presence of the static surround vertical grating ("vestibular + visual"), and 3) rotation of the vertical grating while the platform was motionless, producing simulated optic flow ("visual"). Trials from these three conditions were distributed pseudo-randomly throughout the recording session.

Single-unit recordings

Three mice were chronically implanted in the right RSP with the Neuropixels (phase3A, option 1 and 2, 384 channels) (Jun et al., 2017) and 2 with the Neuronexus probe (Poly2, 32 channels). All acute recordings were made with the Neuropixels probe (phase3A, option 1, 2, and 3). Prior to each insertion, the probe shank was coated with DiI (1 mM, Thermo Fisher Scientific) to allow post hoc histological reconstruction of the probe track (Figures 1B and 1C). Dura was left intact and the craniotomy was covered with saline while the probe was lowered at a speed of 2 μm/s to the desired depth using the stereotaxic manipulator (Kopf Instruments) or micromanipulators (SM-8, Luigs and Neumann). For acute recordings, the craniotomy and the Ag/AgCl ground pellet (1 × 2.5 mm, World Precision Instruments) were then submerged in a 2% agarose (in saline) solution and the probe was allowed to settle for at least 15 minutes before recording started. For chronic implants, the craniotomy was sealed with a silicone sealant (Kwik-Cast, World Precision Instrument). Mice with chronic implants were allowed a minimum of 5 days of recovery from surgery before recordings started and underwent 2 – 3 recording sessions. Successive recording sessions were separated by a minimum time interval of 3 days. At the end of recordings, probes were retracted from the brain, submerged in 1% Tergazyme (in distilled water, Alconox) for at least an hour, and further rinsed with distilled water. For chronic implants, the brain underwent fixation by transcardial perfusion before the probe was retracted.

Extracellular potentials were acquired using an FPGA card (KC705, Xilinx) or the Whisper system (Janelia Applied Physics and Instrumentation Group), and spikeGLX was used as the data acquisition software (https://github.com/billkarsh/SpikeGLX, Janelia Research Campus). For Neuronexus recordings, data were amplified with a gain of 200, filtered at 0.1 – 10000 Hz, and digitised to 16 bits at 25 kHz. For Neuropixels recordings, signals were amplified with a gain of 500, high-pass filtered at 300 Hz, and digitised to 16 bits at 30 kHz.

To isolate single units, data were band-pass filtered (300 – 5000 Hz), and the median of each channel was subtracted to remove any baseline offset. Correlated sources of noise were then removed by common (median) average referencing in blocks of 77 (Neuropixels) or 32 (Neuronexus) channels. Automated spike sorting was carried out using Kilosort (https://github.com/cortex-lab/KiloSort, (Pachitariu et al., 2016)) or KiloSort2 software (https://github.com/MouseLand/Kilosort, (Steinmetz et al., 2021)) with further manual curation of the isolated units using Phy (https://github.com/cortex-lab/phy). Spike sorting parameters are detailed in Tables S1 and S2. Units were excluded if they had < 900 spikes (minimum firing rate = 0.2 Hz), absolute refractory period of < 1 ms, significant amplitude drift across the recording session, and atypical waveforms (noise-like or only positive potentials).

Determining recording location of single units

At the end of the recording, animals were deeply anaesthetised with 120 mg/kg pentobarbitone and transcardially perfused with chilled heparinised phosphate buffer (10 U/ml in PB 0.1 M) and 4% paraformaldehyde (PFA) in PB (0.1 M). Following another 24 hours of fixation in 4% PFA, the brain was extracted and either embedded in 4% agar for automated whole-brain imaging or cut coronally into 100 μm sections using a vibratome (Microm HM 650V, Thermo Scientific). Coronal sections were mounted in a medium containing DAPI (Santa Cruz Biotechnology) and imaged with an epifluorescence microscope (Axio Imager 2, Zeiss). Automated whole brain imaging was performed using serial two-photon tomography. Acquired images were either warped manually into matched sections in the Allen Mouse Brain Atlas (Wang et al., 2020), or by using a validated registration pipeline implemented within the cellfinder software (https://github.com/brainglobe/cellfinder, (Niedworok et al., 2016; Tyson et al., 2021)). The probe track was identified by DiI fluorescence and reconstructed manually using drawing tools in Fiji (Schindelin et al., 2012). The end of the track was determined as the point where DiI fluorescence was no longer visible. This tip location closely matched the probe depth acquired from manipulator readings. By measuring distances from the probe tip and using the geometrical configuration of the probe, the anatomical location of all recording sites along the track was determined. To increase accuracy, these measurements were further compared with electrophysiological signatures along the probe track (i.e., the lack of activity in the white matter or the change in signal-to-noise ratio at the interface of brain and solution), and adjusted accordingly. To identify the location of isolated units along the probe, an average waveform (first 100 spikes) was generated and the recording channel with the largest negative peak was determined.

Single-unit tracking

To identify the same units between freely moving and head-fixed recordings, we adopted previous approaches by matching single units between two discontinuous recordings (Campbell et al., 2018; Ravassard et al., 2013). To allow objective reproducibility, we developed a semi-automated single-unit matching pipeline that allowed identifying same units between the two recording sessions (Figure S3). Spike sorting was carried out separately on the two recordings and for each isolated unit in the head-fixed data (here defined as "Fix"), candidate matches in the freely moving recording (here defined as "Free") was chosen from either eight neighboring channels when using the Neuropixels (four in each direction, maximum 40-μm vertical distance), or four when using the Neuronexus probe (two in each direction, maximum 50-μm distance, Figure S3D). In addition to this, a threshold was placed on the relative "Fix"/"Free" unit firing rates whereby the ratio between the firing rate of a given unit and its potential match must not differ by more than a factor of 20. A similarity score was then calculated for all "Free" units on these neighboring channels based on three categories of similarity metrics derived from the average spike waveform and and inter-spike interval (ISI) distributions:

ISI shape

For each "Fix" unit and its candidate "Free" matching units, the ISI histogram was obtained from the entire duration of the experiment. The following two comparative parameters were then calculated: 1) *ISI histogram correlation*, defined as the Pearson's r of "Fix" versus "Free" ISI histograms. 2) *ISI histogram intersection*, defined as the intersection ratio between "Fix" and "Free" ISI relative frequency histograms calculated as:

$$\frac{\sum_{i=1}^{nBin}\min(ISI_{free}(i), ISI_{fix}(i))}{\sum_{i=1}^{nBin}\max(ISI_{free}(i), ISI_{fix}(i))} \quad (1)$$

Where ISI_{fix} and ISI_{free} are the ISI relative frequency histograms of the "Fix" and the candidate "Free" matching unit, respectively.

Local spike features

Four parameters were used to quantify the difference between specific features of the average "Fix" and "Free" waveforms, including the difference in: 1) *the height of the 2nd peak*, defined as $F(B_{fix}, B_{free})$, 2) *trough-to-peak duration*, defined as $F(C_{fix}, C_{free})$, 3) *trough-to-peak amplitude*, defined as $F(B_{fix}\text{-}D_{fix}, B_{free}\text{-}D_{free})$, 4) *peak-to-trough amplitude*, defined as $F(A_{fix}\text{-}D_{fix}, A_{free}\text{-}D_{free})$.

Where A is the maximum amplitude of the first positive peak preceding the trough; B the maximum amplitude of the second positive peak following the trough; C the time between the minimum of the initial trough and the maximum of the following peak; D the minimum amplitude of the initial trough; and F(x,y) the proportional difference function given by the following equation:

$$F(x,y) = max\left(0, 1 - \left|\frac{x-y}{x}\right|\right) \quad (2)$$

Global spike features

The following three parameters were calculated to compare the entire average spike waveform (4 ms window, from −160 μs to 240 μs relative to the trough) between the "Fix" and the candidate "Free" unit: 1) *spike waveform histogram intersection,* defined as the intersection ratio between "Fix" and "Free" histograms of the amplitude of the average spike waveform (3-μV bins) calculated as in Equation (1). To quantify the temporal similarities between the two waveforms, the following three parameters were calculated by first applying dynamic time warping (DTW, (Salvador and Chan, 2007)) to the average spike waveforms using the fastdtw package (https://github.com/slaypni/fastdtw). 2) *spike waveform difference,* defined as the maximum Euclidean distance between the dynamic time warped "Fix" and "Free" average spike waveforms (normalized by the peak-to-through amplitude). 3) *spike waveform correlation*, defined as the Pearson's r of "Fix" versus "Free" dynamic time warped waveforms. 4) *DTW scale factor,* defined as the ratio of the length of the original "Fix" average spike waveform to the length of the signal after DTW, so as to penalize excessive signal warping.

Within each of the aforementioned categories, the L2 norm of the categories' metrics was calculated, thus generating three similarity metrics. Empirical weights for these similarity metrics (W_{local} = 1/9, W_{global} = 4/9, W_{ISI} = 4/9) were then decided by visual inspection of waveforms and ISI distributions on a subset of data (n = 15 cells) by a user who was blind to the tuning properties of isolated units. The final similarity score was calculated by summing the three weighted metrics. For each "Fix" unit, the "Free" unit with the largest similarity score was identified as the best potential match. If a given "Free" unit was identified as the best potential match of more than one "Fix" unit, it was only assigned to the one with which it had the highest similarity score. At the final step, the best potential match was accepted as the matching "Free" unit if the following thresholds were met: ISI histogram correlation > 0.7, all four local spike features > 0.7, spike waveform correlation > 0.95, spike waveform difference < 0.3. Similar to metrics' weights described above, these thresholds were decided empricially by visual inspection of a subset of data (n = 15) via a graphical user interface.

Single-unit classification

K-means clustering (with k = 2) was used to classify the isolated units as wide or narrow spiking based on features of their average waveform at the recording site with the largest amplitude. Two metrics were used for this classification: the height of the second positive peak relative to the initial trough, and the time between the minimum of the initial trough and the maximum of the following peak.

To investigate whether wide- and narrow-spiking cell classes correspond to excitatory and inhibitory cell types, respectively, we next performed cross-correlogram (CCG) analysis to identify putative monosynaptic connections between neurons (Barthó et al., 2004). Excitatory and inhibitory connections were identified as short-latency and short-duration peaks or troughs in the CCGs. The baseline firing rate of each 0.5-ms CCG bin (−50 to 50 ms) was first determined by applying a Fourier smoothing with a frequency cut-off at 5 kHz. A confidence band was then calculated from the 0.0001–99.9999 percentile of the cumulative Poisson distribution at each time bin, and used as the statistical threshold for detecting outliers at 1.5 to 4 ms time window from the center bin. A significant peak, indicating an excitatory interaction, exceeded the upper limit of the confidence band in at least two bins. A significant trough, indicating an inhibitory interaction, was below the lower limit of the confidence band in at least three bins. Cell type assignment using K-means clustering was then evaluated for the subset of units identified as excitatory and inhibitory based on CCG interactions, and the two were found to be largely overlapping (93.3% overlap).

Pupil tracking

The right pupil was recorded at 40 fps using a near-IR camera (acA640-750um, Basler AG) and a custom program written in C++ based on the OpenCV and Pylon 5 libraries (https://www.baslerweb.com/en/sales-support/downloads/software-downloads,(Vélez-Fort et al., 2018). An ITC-18 interface board (InstruTECH, Heka Elektronik) and Igor Pro were used to control camera triggering and synchronization with rotation stimuli. Illumination was provided by an array of infrared LEDs (Kingbright, 940 nm) and the pupil was focused using two lenses (f1 = 25 mm, f2 = 75 mm, Thorlabs). Pupil movements were then tracked offline using DeepLabCut (DLC, (Mathis et al., 2018)). A pre-trained ResNet-50 network was trained on 240 frames from 6 video recordings (40 frames from each) with 500000 training iterations, reaching a final loss of 0.0007 and a training and testing error of 1.7 and 4.1 pixels, respectively. To identify rapid eye movement events, the differential (central derivative) of the horizontal eye position over time was calculated and a median filter (50-ms window) applied to attenuate noise. Outliers were removed by using a threshold cut-off of 20 mm/s and a Lowess smoothing (span = 0.01)

was applied to subtract low frequency fluctuations. Rapid eye movement events were then detected using a threshold of 2.5 × SD. For each isolated unit, the number of spikes that occurred during nasal or temporal eye movement events was obtained (from 75 ms before event onset to 250 ms after) and the average spiking rate histograms (25-ms bins) constructed. Neurons were considered to be modulated by eye movements if their average spiking rate was significantly correlated (Pearson's r test) with the average amplitude of eye movement events at either nasal or temporal direction.

Vestibular lesion assessment

Mice were allowed 4 – 11 days to fully recover from the vestibular lesion surgery before behavioral and single-unit recordings were made. All lesioned mice showed body curling when held by the base of the tail. Further vestibular deficits were quantified by recording the animals' trajectory while exploring a 39-cm diameter circular arena in the dark using Raspberry Pi 1B, a Pi NoIR camera (30 fps) and a custom-written routine in Python (https://github.com/SainsburyWellcomeCentre/Pyper, (Vélez-Fort et al., 2018)). The animal's trajectory was recorded both before the lesion surgery and after full recovery. The Cartesian coordinates of the centroid of the mouse were determined for each frame, and turning angle was quantified by calculating the change in trajectory in the horizontal plane using coordinates from three consecutive frames. The distribution of turn angles over a set distance was then compared between pre- and post-lesion recordings.

Rotation discrimination task

All behavioral experiments were performed on 6-week old mice. Animals were allowed to recover for at least two days from headplate implant surgery before training began. They were then given restricted access to water for another two days and habituated to head-fixation on the rotating platform. The head was positioned over the center of the axis of rotation as above and a water reward port was positioned in front of the animal. Mounted on the same platform was a roofed Perspex cylinder (radius = 12 cm) that completely surrounded the animal. The outside of the cylinder was coated with a black projection film onto which the visual stimulus was projected. The entire rotation platform was housed inside an acoustically and optically isolated chamber.

Starting with the "vestibular" training, mice were rotated 90° clockwise in the dark over a period of 32.2 s with a peak velocity of 80°/s (S+ stimulus, Figures 4A and 4B), and for at least 100 trials (inter-trial interval = 5 s). Licking for two or more 250-ms time bins after the peak velocity (16.1 s from rotation onset) yielded a water reward of approximately 5 μl, and was scored as a correct S+ response. Once mice demonstrated licking in more than 80% of S+ trials for at least 100 trials, the S- stimulus was introduced. The S- stimulus had a peak velocity of 10°/s, identical onset and offset times and area under the curve to the S+ stimulus (Figure 4B), and was not rewarded. Licking for fewer than two 250-ms bins after the peak velocity of S- stimulus was recorded as a correct S- response. Mice were pseudo-randomly presented with 10 S+ and 10 S- trials in blocks of 20 trials, and performed 5 – 15 blocks per day. The percentage of correct responses was determined for each block, and discrimination accuracy was measured as the sum of the percentage of correct S+ and S- trials, divided by two. Once mice reached a criterion of 80% discrimination accuracy on average for at least 5 consecutive blocks, and performed a minimum of 20 blocks, the S+ stimulus peak was reduced incrementally by 5 – 10°/s every 5 blocks until the S+ and S- stimuli were identical.

Next, mice were tested in the "visual" experimental condition similar to the recording paradigm above. The platform remained motionless and a vertical grating was presented on to the projection film using the laser projector and moved around the mouse. Here, the projector was mounted on a post attached to the rotation motor, and the grating (azimuth = 56°, altitude = 50°) was physically rotated 90° in the CCW direction starting at 45° to the right of the head's midline. Mice were trained to discriminate between pairs of rotating visual stimuli, with speed profiles identical to S+ and S- vestibular stimuli described above. After performing at least 20 blocks on the stimulus pair consisting of an 80°/s peak velocity (S+) and a 10°/s peak velocity (S-), the peak speed of the S+ stimulus was again reduced by 5 – 10°/s every 5 blocks until the two stimuli were identical. Finally, under the "vestibular + visual" condition, the visual stimulus remained static and the mouse was rotated as in the "vestibular" condition. To test whether the structure of task progression from "vestibular" to "vestibular + visual" experiments resulted in the observed improved performance under the multisensory condition, all mice were tested under the "vestibular" condition again using the rotation stimulus with peak velocity of 30°/s as S+ (Figure S7).

To compare performance between experimental conditions, for each condition, discrimination accuracies from all mice and for the three stimulus pairs that were tested under all experiments (S+ peak = 20°/s, 30°/s, and 80°/s) were grouped. Group means were then compared using one-way ANOVA followed by the Holm-Sidak multiple comparisons test.

QUANTIFICATION AND STATISTICAL ANALYSIS

Open field analysis

Behavioral variables were extracted from video frames using DLC. A pre-trained ResNet-50 network was trained on 1190 frames from 8 video recordings (40 – 70 frames from each) with 700000 training iterations, reaching a final loss of 0.0009 and a training and testing error of 1.9 and 2.8 pixels, respectively. Head direction and AHV were calculated from tracked ear positions (horizontal plane, top view). Locomotion speed was calculated from tracked body position (Figure 1A). Cells with average firing rate < 0.5 Hz over the entire experiment duration were excluded from the analysis. For the analysis of head direction tuning, recording epochs in which the animal's speed was below 1.5 cm/s were excluded. This speed cut-off was not used for the analysis of speed or AHV tuning. Tuning curves were computed separately for each experimental condition (light1, dark, light2) with the same recording length used across conditions.

Head direction was defined as the angle between the horizontal axis and the line perpendicular to the axis joining the ears. To determine head direction and AHV tuning, first head direction time series was smoothed with a sliding mean filter (50 ms width). For each neuron, the average firing rate as a function of head direction, binned at 6°, was then calculated as the total number of spikes divided by the total time that the animal's head occupied each head direction bin. The mean Rayleigh vector length of the head direction tuning curve was computed and the Rayleigh test was performed to assess non-uniformity using pycircstat (https://github.com/circstat/pycircstat). Neurons were classified as head direction tuned if under both light conditions (light1 and light2), the distribution of their firing rate as a function of head direction was statistically non-uniform (Rayleigh p value < 0.01) and their Rayleigh vector length was > 99th percentile of the mean vector length in the null distribution. The null distribution was determined by a shuffling procedure based on all recorded neurons with 1000 permutations performed for each cell. For each permutation, the entire sequence of spikes was shifted by a random amount between 20 s and the total duration of recording minus 20 s, and the mean vector length calculated from the shuffled head direction tuning curve. The 99th percentile threshold came to 0.19, consistent with previous reports in mice (Giocomo et al., 2014).

To construct AHV tuning curves, for each time point on the smoothed head direction times series, the angular velocity was calculated by determining the first derivative over a 200-ms time window ending on that time point. The firing rate was then plotted as a function of angular velocity binned at 6°/s. To allow comparison with passive rotation experiments, we used a maximum angular velocity of 80°/s to construct the AHV tuning curves. Positive velocities were assigned to right and negative velocities to left head turns. For each cell, two AHV scores were calculated for right and left head turns, defined as the magnitude of correlation (absolute Pearson's r) between the firing rate and the angular velocity. AHV slopes were calculated by applying a linear fit to the right-turn and left-turn firing rate-AHV functions. Cells were classified as AHV tuned if either of the AHV scores was > 95th percentile of the null distribution (Campbell et al., 2018; Kropff et al., 2015; Preston-Ferrer et al., 2016). The null distribution was based on each cell and obtained by a similar shuffling procedure as above with 1000 permutations. To compare the AHV tuning curves between light and dark conditions, neurons that met the above criterion during either dark or light1 session were classified as AHV cells.

To identify cells tuned to linear locomotion speed, the position of the mouse in each video frame was estimated in Cartesian coordinates and the instantaneous locomotion speed calculated as the distance traveled between two consecutive frames divided by the camera sampling rate (25 ms). Locomotion speed time series was then smoothed with a sliding mean filter (50 ms width) and for each cell, the average firing rate as a function of speed, binned at 1 cm/s, was calculated as the ratio between spike counts and the time spent in each speed bin. Locomotion speeds above 20 cm/s were excluded from the analysis due to low sample sizes at high speeds. Neurons were classified as speed tuned if their speed scores (absulote Pearson's r between the cell's firing rate and the animal's locomotion speed) was > 95th percentile of the null distribution, generated for each cell by a shuffling procedure as described above with 1000 permutations.

To compute stability indices for AHV- and speed-tuned cells, recording sessions were divided into two halves and the magnitude of correlation (Pearson's r) between tuning curves from each half was calculated. Shuffled distributions (Figure S1D) were obtained by randomly shifting all the spikes in each half-session between 20 s and the full duration minus 20 s.

To assess the degree of theta rhythmicity in spiking of recorded neurons, spike train autocorrelograms, binned at 1 ms, were computed for temporal lags of up to ± 500 ms. The peak of the autocorrelogram at zero lag was equalized to the maximal value excluding the zero-lag peak, and the mean was subtracted. The power spectrum of the autocorrelogram was computed as the square of the magnitude of the fast Fourier transform (FFT) of the autocorrelogram, and zero-padded to 2^{16} samples. The power spectrum was then smoothed with a 2-Hz mean window and the peak within 5-11 Hz range was identified. Theta-modulation index was measured as the ratio of this theta-range peak to the mean power between 0 and 50 Hz. A neuron was defined as significantly theta modulated if its theta index was at least 5 (Yartsev et al., 2011).

Rotation analysis

The analysis procedures outlined below were applied similarly to data obtained under all three experimental conditions, thus the term "rotation" refers to both "vestibular" and "visual" stimuli. To construct rotation velocity tuning curves, for each neuron, the average firing rate as a function of rotation velocity, binned at 5°/s, was calculated as the trial-averaged number of spikes divided by the total duration of each velocity bin. Two rotation velocity scores (CW and CCW) were calculated for each neuron, defined as the magnitude of correlation (absolute Pearson's r) between the trial-averaged firing rate and the rotation velocity. Neurons were defined as modulated by rotation velocity if either of the rotation velocity scores was > 95th of the null distribution. The null distribution was based on each cell and obtained by shuffling the firing rates across rotation velocity bins with 1000 permutations.

Stimulus-evoked responses were defined as significant increases or decreases in the average firing rate during either CW or CCW rotations as compared to the preceding stationary period of the same duration. Direction-modulated cells were defined as those with a significant difference between CW and CCW firing rates. In both cases, statistical significance was determined with the Wilcoxon signed-rank test. Rotation modulation index was defined as:

$$\frac{|\overline{R}_{rot} - \overline{R}_{base}|}{\overline{R}_{base}} \quad (3)$$

Where $\overline{R}_{rot}$ and $\overline{R}_{base}$ are trial-averaged (10 – 15 trials) firing rates during either CW or CCW rotations and during the stationary period, respectively.

Direction selectivity index (Figures 3A and 3B) was defined as the area under the receiver operating characteristic (ROC) curve that compared the distribution of CW versus CCW firing rates. These values ranged between 0 and 1 and not rectified (see ROC analysis).

To construct the firing rate heatmaps (Figure 2F, Figure 3A-B), trial-averaged firing rate of each cell was calculated, binned either at 200 ms (temporal heatmaps) or 5°/s (speed heatmaps), and normalized to the peak. The median firing rate of the preceding stationary period was then subtracted. For speed heatmaps, firing rates at CW and CCW directions were calculated separately and presented on the same plot in two consecutive rows.

To compare angular velocity tuning of neurons tracked between freely moving and head-fixed recordings, for each neuron, the average firing rate at each AHV bin (''active'') was plotted against the average firing rate at the corresponding rotation velocity bin (''passive,'' Figure 2C). Cells were defined as similarly tuned if the correlation (Pearson's r) between the ''active'' and ''passive'' firing rates was > 95th percentile of the null distribution, computed for each cell by shuffling firing rates across AHV bins with 1000 permutations.

ROC analysis

We performed ROC analyses using the pROC package of R (Robin et al., 2011) to determine whether individual neurons could discriminate the direction (CW v. CCW, direction discrimination) or the speed of rotations (10°/s v. 15°/s – 80°/s, speed discrimination). To construct the speed ROC curves for each neuron, the firing rate as a function of rotation speed (absolute velocity), binned at 5°/s, was first calculated for each trial as the ratio between spike counts and the time spent in each speed bin. Speed ROC curves were then calculated by comparing the firing rate distribution of the speed bin that peaked at 10°/s (5°/s – 10°/s bin) versus the successive fourteen speed bins, peaking at 15°/s to 80°/s. Direction ROC curves compared the firing rate distribution of CW versus CCW rotations. We computed the area under the ROC curve (AUC) as a measure of neuron's direction and speed discriminability. AUC values lower than 0.5 were rectified, so that all AUCs were between 0.5 and 1. To test whether discriminability was significantly higher than expected by chance, for each cell, we computed the 99% CI of the AUC values using the Delong method (DeLong et al., 1988). The AUC was considered significant if the lower bound of this 99% CI was > 0.5 (chance).

Population decoding

Linear discriminant analysis (LDA) was used to quantify how effectively population of RSP neurons encode the direction and speed of angular motion under the three experimental conditions. This analysis was performed with the scikit-learn module (Pedregosa et al., 2011) using Eigenvalue decomposition and applying shrinkage. LDA was used to quantify how well RSP populations could discriminate between rotation directions (CW v. CCW) or between pairs of rotation speed calculated from the firing rate-speed tuning function described above (speed bin peaking at 10°/s v. speed bins peaking at 15°/s – 80°/s). For each neuron, we selected 10 trials per stimulus condition, resulting in a total of 60 trials for all three experimental conditions (''vestibular,'' ''vestibular + visual,'' ''visual''). We applied LDA to decode the direction and speed of each trial from the firing rates of all neurons in the population, using a balanced cross-validation method for training and testing. When decoding was performed on all six conditions (2 stimulus conditions × 3 experimental conditions, Figures 6C and 6D), 54 trials were used for training the decoder and 6 for testing, with a different set of trials used each time for testing. Similarly, when decoding was performed on 2 conditions (2 stimulus conditions × 1 experimental condition, Figures 6A and 6B), 18 trials were used for training and the remaining 2 for testing. Before training, we z-scored all firing rates for each neuron, with no pre-selection applied based on neuron's responses to stimuli or inhibitory/excitatory cell type assignments. Decoding accuracy was computed as the number of correctly decoded trials divided by the total number of correctly and incorrectly decoded trials. To create pseudo-populations, trial simultaneity among neurons was allocated between trials of the same stimulus and experimental condition. A bootstrap procedure was used to create pseudo-populations of increasing size and to calculate the mean decoding accuracy in each pseudo-population (Figure 6). RSP neurons from all recording sessions (or tracked AHV cells) were sampled with replacement to generate 1000 bootstrap samples with the same number of neurons. LDA was then performed on each bootstrap sample, generating 1000 measures of decoding accuracy, and the mean decoding accuracy was computed across all bootstrap measures. To test whether the performance of the decoder improved under ''vestibular + visual'' compared to ''vestibular'' condition, for each experimental condition, mean decoding accuracies obtained from pseudo-populations of different sizes were grouped and group means compared using one-way ANOVA followed by the Holm-Sidak multiple comparisons test. To obtain a single measure of speed decoding accuracy for each pseudo-population, accuracies from all speed pairs were averaged.

The same decoding method was used on real RSP populations composed of simultaneously recorded neurons. Simultaneous populations containing a minimum of 10 or 20 neurons were used for direction and speed decoding, respectively. These thresholds were obtained from the pseudo-population analysis described above, where we determined the minimum population size required to achieve a mean decoding accuracy of above 70% under the ''vestibular'' condition.

Statistics

For data analysis, we developed open-source pipelines in Python 3.6 using numpy (Harris et al., 2020), scipy (Virtanen et al., 2020), pandas (Reback et al., 2020), matplotlib (Hunter, 2007), and seaborn (Waskom et al., 2020) libraries, in addition to other packages described above. The open field analysis code is available at: https://github.com/adamltyson/opendirection (DOI in the Key

Resources Table). The rest of single-unit analysis pipeline including single-unit classification, single-unit tracking, rotation and eye-movement analysis, and comparison of freely moving versus head-fixed data is available at: https://github.com/RichardFav/spikeGUI (DOI in the Key Resources Table). Statistical comparisons were performed using the stats package in R or GraphPad Prism. Unless stated otherwise, statistical significance is defined as $p < 0.05$. Data were subjected to a test of normality with the Agostino & Pearson test or Shapiro-Wilk test, and non-parametric statistics were applied to data with non-normal distributions. Statistical details are provided in the main text or in figure legends.

Neuron, Volume *110*

Supplemental information

Multisensory coding of angular head velocity in the retrosplenial cortex

Sepiedeh Keshavarzi, Edward F. Bracey, Richard A. Faville, Dario Campagner, Adam L. Tyson, Stephen C. Lenzi, Tiago Branco, and Troy W. Margrie

Table S1. Parameters used for automated spike sorting with KiloSort. Related to STAR Methods.

ops.Nfilt	640*
ops.whitening	full
ops.nSkipCov	1
ops.whiteningRange	32
ops.criterionNoiseChannels	0.1
ops.Nrank	3
ops.nfullpasses	6
ops.maxFR	20000
ops.fshigh	300
ops.ntbuff	64
ops.scaleproc	200
ops.Th	[4 10 10]
ops.lam	[5 20 20]
ops.nannealpasses	4
ops.momentum	1./[20 400]
ops.shuffle_clusters	1
ops.mergeT	0.1
ops.splitT	0.1
ops.initialize	fromData
ops.spkTh	-4
ops.loc_range	[3 1]
ops.long_range	[30 6]
ops.maskMaxChannels	5
ops.crit	0.65
ops.nFiltMax	10000

* Neuronexus Poly2 = 64

Table S2. Parameters used for automated spike sorting with KiloSort2. Related to STAR Methods.

ops.fshigh	300
ops.minfr_goodchannels	0
ops.Th	[10 4]
ops.lam	10
ops.AUCsplit	0.85*
ops.minFR	1/50
ops.momentum	[20 400]
ops.sigmaMask	30
ops.ThPre	8
ops.spkTh	-6†
ops.nfilt_factor	4
ops.ntbuff	64
ops.whiteningRange	32
ops.nSkipCov	25
ops.scaleproc	200
ops.nPCs	3

* Neuronexus Poly2 = 0.6

† Neuronexus Poly2 = -3

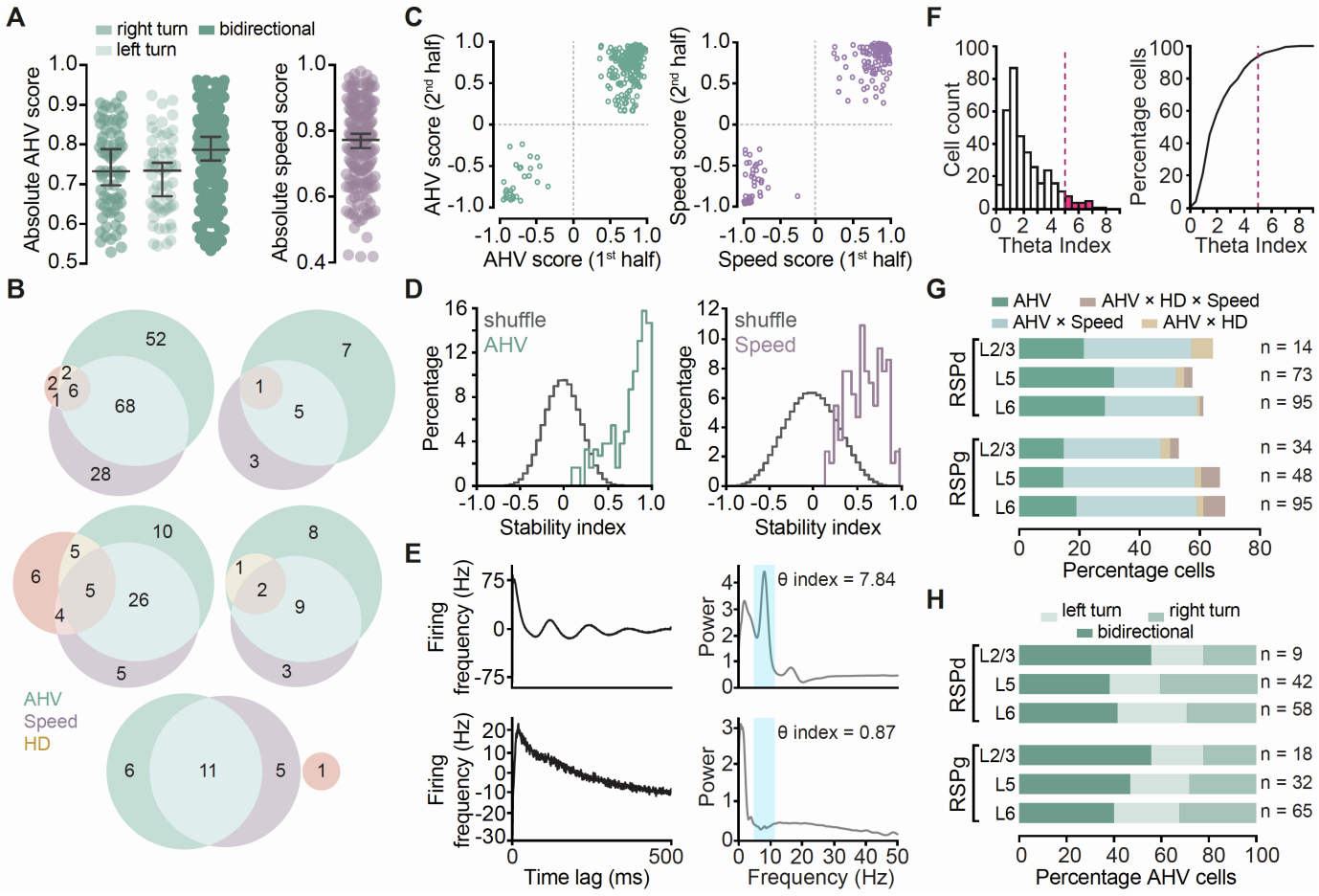

Figure S1. Tuning Properties of RSP neurons recorded during free exploration. Related to Figure 1.

A, Magnitude of AHV (left) and speed (right) scores, defined as absolute Pearson's r of correlations between a cell's firing rate and AHV or linear locomotion speed. Each circle represents a tuned cell. Black lines and error bars are median and 95% CI. Neurons with bidirectional AHV tuning (dark green) are represented by two circles for the two turning directions. Neurons with unidirectional AHV tuning are shown in transparent green shades (right turn or left turn) **B**, Venn diagrams showing cells tuned to head direction (HD), AHV, and linear locomotion speed in each mouse. **C**, AHV (left) and speed (right) scores from the first half of the recording session plotted against that of the second half for each tuned cell (AHV Spearman rho = 0.6, p <1e-15; Speed Spearman rho = 0.72, p <1e-15). **D**, Distribution of stability indices for AHV (left, green) and speed (right, purple) tuned cells versus shuffled distributions (grey). **E**, Autocorrelogram (left, bin size = 1 ms) and power spectrum (right) of a theta modulated cell (top) and a cell with no theta rhythmic firing (bottom). Blue window defines 5 - 11 Hz theta range. **F**, Left: frequency distribution of theta indices for all RSP neurons recorded in the open field. Pink bars show the number of theta modulated cells. Right: cumulative distribution of theta indices in the population. Approximately 94% of RSP cells did not show theta rhythmic firing. Dashed lines delineate the cut-off for a significant theta index. **G**, Percentage of AHV tuned neurons across RSP regions and layers. n, number of recorded neurons in each layer. **H**, Percentage of AHV cell types across RSP regions and layers. n , number of AHV tuned neurons in each layer.

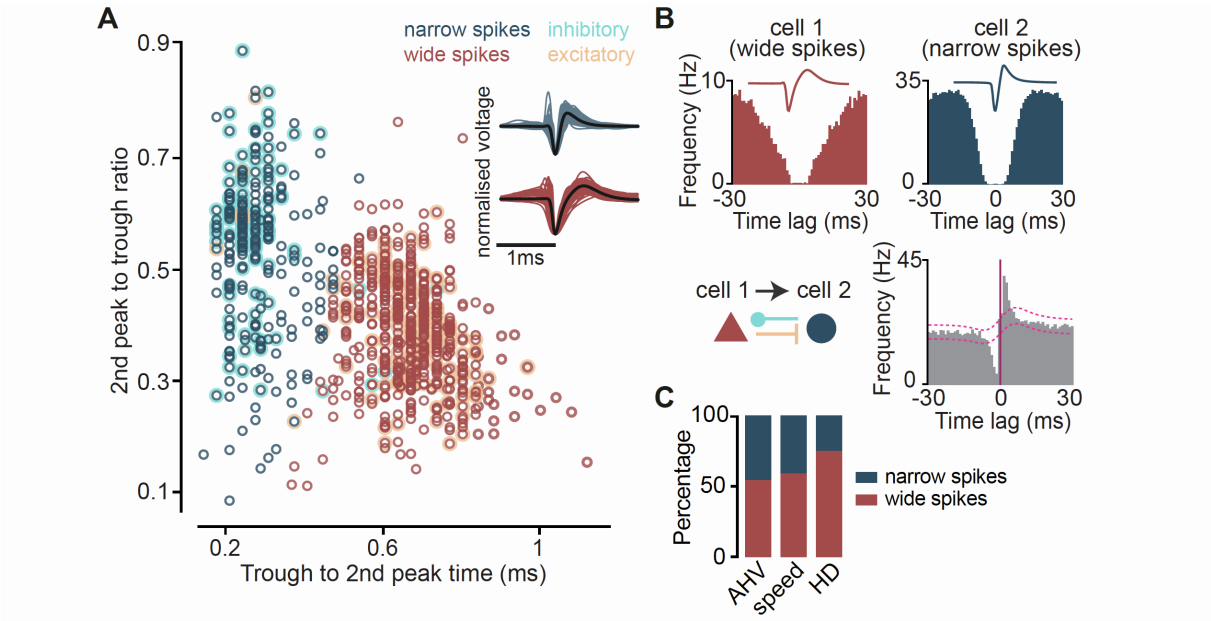

Figure S2. Both excitatory and inhibitory neurons in the RSP represent AHV. Related to Figure 1.

A, K-means clustering of isolated RSP units based on spike width and peak/trough ratio. Single units were separated into two clusters with wide (putative excitatory, n = 460, 68%, red) and narrow (putative inhibitory, n = 216, 32%, dark blue) spikes. Cyan and orange circles mark neurons identified as inhibitory and excitatory based on cross-correlogram (CCG) analysis. **B**, Top: average spike waveform and auto-correlogram of two example single units with wide and narrow spikes. Bottom: schematic of reciprocal monosynaptic connections (left) based on the CCG for the same pair (right). Dashed lines indicate 99.98% confidence interval. **C**, Percentage of putative excitatory (wide spikes) and inhibitory (narrow spike) neurons among AHV (n = 224), speed (n = 182), and HD (n = 36) tuned cells.

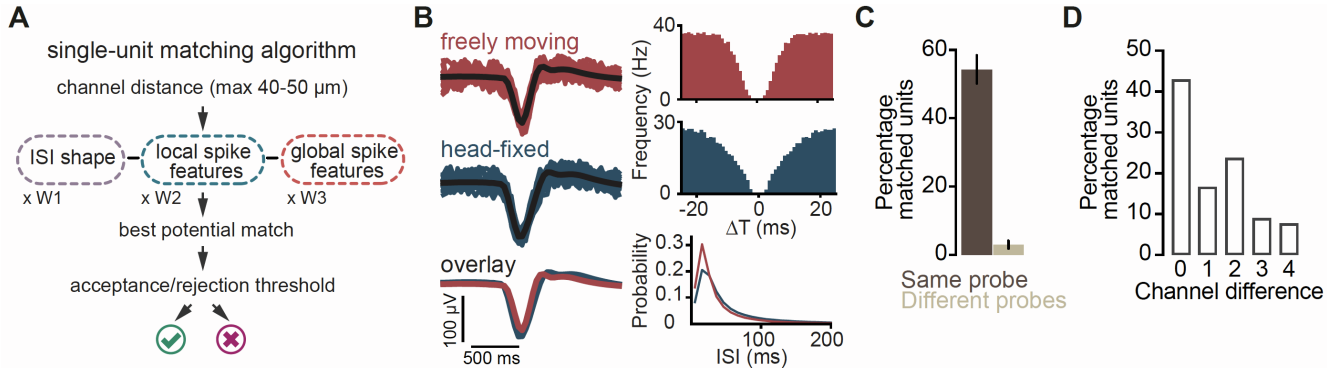

Figure S3. Tracking single units between freely moving and head-fixed recordings. Related to Figure 2.

A, Schematic of the single-unit matching algorithm. Probe geometry and multiple similarity metrics for spike features and inter-spike interval (ISI) distributions were used to find best potential matches. **B**, Example of a single unit tracked between head-fixed (blue) and freely moving (red) sessions. Top- and centre-left: red and blue traces are individual spikes (20 displayed). Black traces show average waveforms from all spikes. Bottom-left: average waveforms superimposed. Right: auto-correlograms (top and centre) and ISI distribution (bottom) of the tracked unit under the two conditions. **C**, Summary data (mean ± SEM, 12 fix-free recording pairs) showing the percentage of head-fixed single units with an accepted match in the freely moving recording (same probe). Control data were generated by applying the same matching algorithm to recordings from different animals (different probes, 10 pseudo-random pairs). **D,** Percentage distribution of head-fixed single units with an accepted match in the freely moving recording located either on the same channel (channel difference = 0) or separated by 1 to 4 channels. Maximum accepted distance was 2 recording channels on the Neuronexus (50 µm) and 4 on the Neuropixels (40 µm vertical) probe.

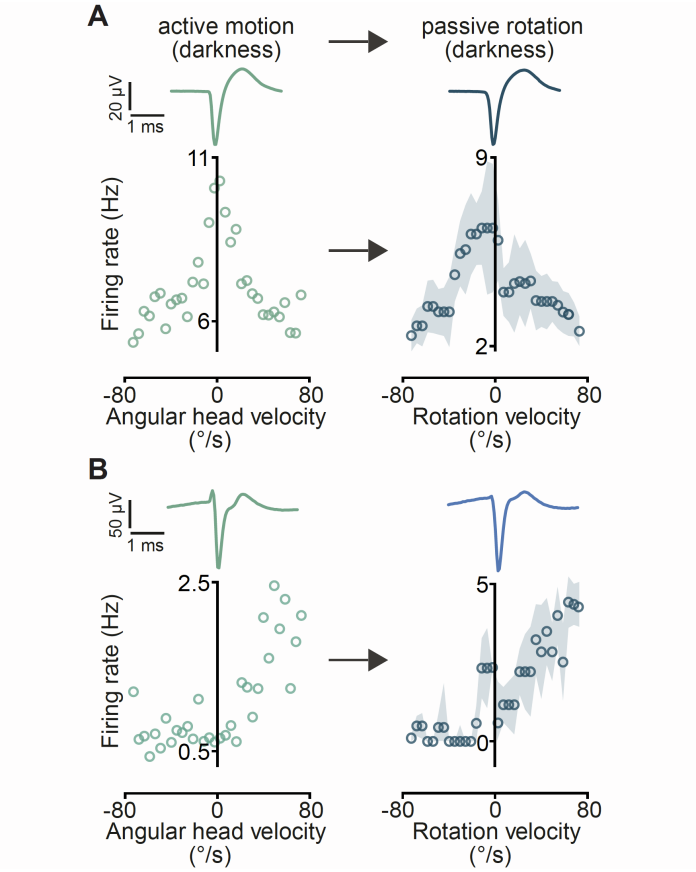

Figure S4. AHV cells maintain their tuning during restrained passive motion. Related to Figure 2.

A, Example of a bidirectional negatively correlated AHV cell, and **B**, a unidirectional AHV cell recorded during both open field exploration (left) and head-fixed passive rotation (right) in darkness. Top traces show average spike waveforms. Circles and shaded area on the right show trial-averaged firing rates (12 trials) and SEM, respectively.

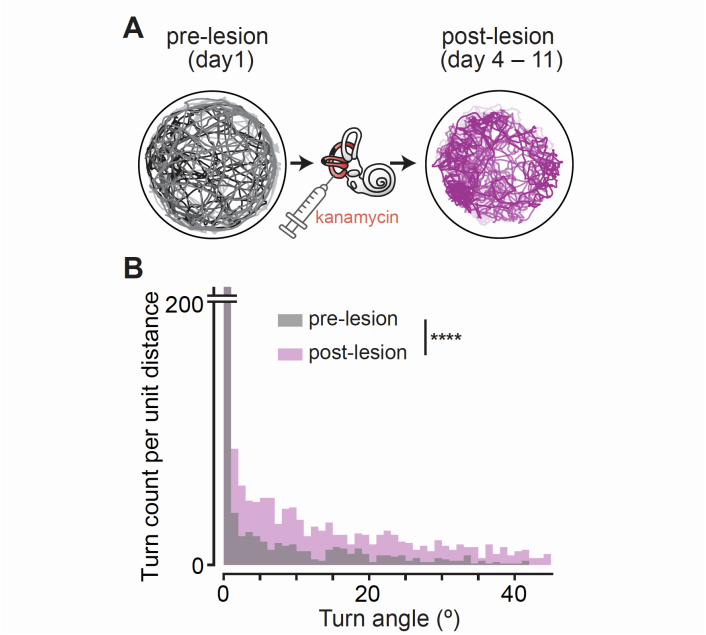

Figure S5. Locomotion and turning behaviour following vestibular lesions. Related to Figure 2.

A, Overlaid open field trajectories of 4 mice before (left) and after (right) bilateral kanamycin-induced lesions of the horizontal and posterior semi-circular canals. **B**, Scaled histogram of turning angles, binned at 1º, for all 4 mice before (grey) and after (pink) vestibular lesions. ****p = 2e-83, Kolmogorov–Smirnov test.

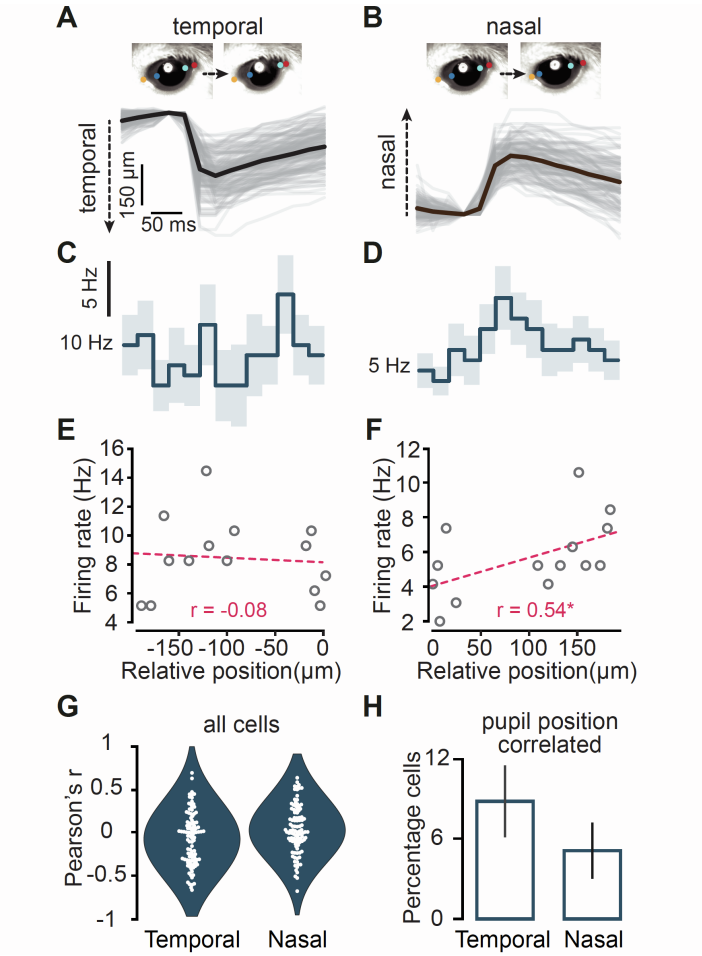

Figure S6. Eye movement-related activities in the RSP recorded during passive rotation. Related to Figure 2.

A-B, Top: video frames showing example temporal (**A**) and nasal (**B**) eye movements recorded at 40 fps in the dark. Coloured circles show marked positions for eye tracking using DLC. Bottom: example individual (grey), and averaged (black) fast eye movement events from one mouse. **C-D**, Mean (lines) and SEM (shades) firing rate histograms of an example cell aligned with detected temporal and nasal eye movements in **A** and **B**. Spiking rates during each eye movement event (from 75 ms before movement onset to 250 ms after) were determined in 25 ms time bins. **E-F,** Mean firing rate of the same cell (**C-D**) at each 25 ms time bin plotted against the averaged relative eye position. Dashed line shows linear fits. *Significant Pearson correlation ($p = 0.048$). **G**, Population data showing magnitude of correlations between firing rate and eye position. Circles represent individual neurons. **H**, Summary data (mean ± SEM) showing proportion of cells with significant eye-position correlations (n = 3 mice, 101 cells, p significance threshold = 0.05).

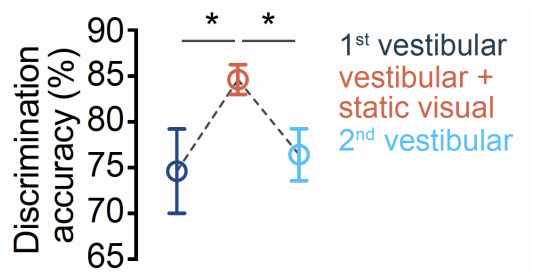

Figure S7. Angular velocity discrimination immediately before and after the addition of a visual cue. Related to Figure 4.

Mean (± SEM) discrimination accuracies for the 30:10 stimulus pair (average of 5 blocks) in all 5 mice tested first in the dark (1st vestibular), then under the multisensory condition (vestibular + static visual), and again under another "vestibular" condition (2nd vestibular). *p (1st vestibular vs. vestibular + visual) = 0.03, *p (2nd vestibular vs. vestibular + visual) = 0.04, one-way ANOVA with Holm-Sidak's test.

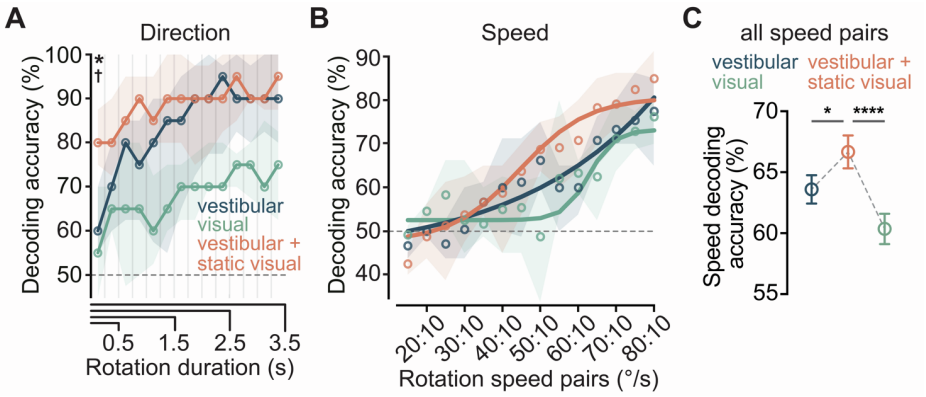

Figure S8. Combination of vestibular and visual stimuli improves decoding of angular self-motion by RSP neuronal populations. Related to Figure 6.

A, Population decoding accuracy for direction as a function of rotation duration. Circles and shaded areas show median and IQRs. Dashed line represents theoretical chance. *p (vestibular v. vestibular + visual) = 0.04, †p (visual v. vestibular + visual) = 0.01, pairwise Wilcoxon signed rank test with Bonferonni correction, first 250 ms, n = 10 mice, 19 recordings, 10 – 84 cells per recording. **B**, Population decoding accuracies for speed. Circles and shaded areas show median and IQRs. Lines are sigmoid fits. n = 7 mice, 12 recordings, 22 – 84 cells per recording. **C**, Mean (± SEM) speed decoding accuracy of all speed pairs. *p = 0.01, ****p = 6.4e-5, one-way ANOVA with Holm-Sidak's test.